Simulation of High Temperature InGaN Photovoltaic Devices

by

Yi Fang

A Dissertation Presented in Partial Fulfillment
of the Requirements for the Degree
Doctor of Philosophy

Approved October 2017 by the
Graduate Supervisory Committee:

Dragica Vasileska, Co-Chair
Stephen Goodnick, Co-Chair
Fernando Ponce
Robert Nemanich

ARIZONA STATE UNIVERSITY

December 2017

ABSTRACT

In recent years, there has been increased interest in the Indium Gallium Nitride (InGaN) material system for photovoltaic (PV) applications. The InGaN alloy system has demonstrated high performance for high frequency power devices, as well as for optical light emitters. This material system is also promising for photovoltaic applications due to broad range of bandgaps of $In_xGa_{1-x}N$ alloys from 0.65 eV (InN) to 3.42 eV (GaN), which covers most of the electromagnetic spectrum from ultraviolet to infrared wavelengths. InGaN's high absorption coefficient, radiation resistance and thermal stability (operating with temperature > 450 °C) makes it a suitable PV candidate for hybrid concentrating solar thermal systems as well as other high temperature applications. This work proposed a high efficiency InGaN-based 2J tandem cell for high temperature (450 ℃) and concentration (200 X) hybrid concentrated solar thermal (CSP) application via numerical simulation. In order to address the polarization and band-offset issues for GaN/InGaN hetero-solar cells, band-engineering techniques are adopted and a simple interlayer is proposed at the hetero-interface rather than an Indium composition grading layer which is not practical in fabrication. The base absorber thickness and doping has been optimized for 1J cell performance and current matching has been achieved for 2J tandem cell design. The simulations also suggest that the issue of crystalline quality (i.e. short SRH lifetime) of the nitride material system to date is a crucial factor limiting the performance of the designed 2J cell at high temperature. Three pathways to achieve ~25% efficiency have been proposed under 450 ℃ and 200 X. An anti-reflection coating (ARC) for the InGaN solar cell optical management has been designed. Finally, effective mobility model for quantum well solar cells has been developed for efficient quasi-bulk simulation.

DEDICATION

I would like to thank my parents for their support and love. To my mom and dad, who raise me, educated me, guided me to pursue my dreams and encourage me to seek the opportunity to study in United States.

I would like to acknowledge all the great friends I have made in Arizona State University. You guys helped me to survive in a foreign country.

I would like to thank fate. I met, felt in love and married my wife, Yawen Zou, here in ASU. We came to United States on the same day and met in a church after arrival. Yawen, thank you for keeping me company and cheering me up during all those dark days.

I would also want to thank Angela. She is a chiwawa dog adopted from a shelter when I was so stressed about my research work. Thank you for bringing me happiness and let me know the weight of responsibility.

ACKNOWLEDGMENTS

First of all, I would like to express my gratitude to my co-advisor Dr. Dragica Vasileska for her patient guidance and continuous support throughout my PhD. Thank you for bringing me into your research group and providing me the opportunity to do research on semiconductor modeling. Your strong and graceful attitude towards life and work has deeply impressed me and made me a better person.

I have to thank my co-advisor Dr. Stephen Goodnick. Thank you for giving guidance on my PHD research in the field of InGaN photovoltaics and shaping me into a better researcher.

I also would like to thank Dr. Fernando Ponce and Dr. Robert Nemanich for serving on my committee and giving valuable suggestions.

Thanks to all my colleagues in Dr. Vasileska's research group. Special thanks go to Da Guo, thanks for your help since I joined this group and so many brainstorming together about my research.

Finally, I gratefully acknowledge the funding support from the ARPA-E FOCUS project.

TABLE OF CONTENTS

Page

CHAPTER Page

LIST OF TABLES

LIST OF FIGURES

Figure Page

Figure Page

Figure Page

Figure Page

CHAPTER 1

INTRODUCTION

1.1 Demands for High Temperature Solar Cell

Renewable energy resources such as solar power have become an attractive topic in the past decades as the necessity of alternative energy solutions for human energy consumption have become increasingly important. Power generated from traditional fossil fuel energy resources such as coal, oil and natural gas will produce environmental pollution as a by-product. First, the mining of these non-renewable energy resources may cause damage to the local ecosystem of the mining area. Second, there is little doubt that carbon dioxide, methane and nitrous oxides formed after fossil fuels consumption, become 'greenhouse gas' and contribute to global warming. Thirdly, when burning fossil fuels, nitrous oxide emissions enhance the damage to the ozone layer and sulphur dioxide is responsible for acid rain.

In contrast, solar energy provides a 'clean' path for human energy consumption. Solar power is the most abundant renewable energy resource among all other renewable and fossil-fuel based energy resources combined. The sun offers ~885 million terra-watt-hours (TWh) that reach the earth's surface in a year, which is ~6200 times of the energy consumed by human activities in 2008 and will be ~4200 times the energy that would be consumed by humankind in 2035 [1]. There are two technologies for solar energy harvesting: concentrated solar thermal systems (CSP) and semiconductor photovoltaics (PV). Solar thermal systems transfer solar power into heat and this heat is utilized to produce steam to spin a turbine. The spinning of generator via working steam finally generates electricity similar to that of concept as fossil fuel and nuclear power plants. The

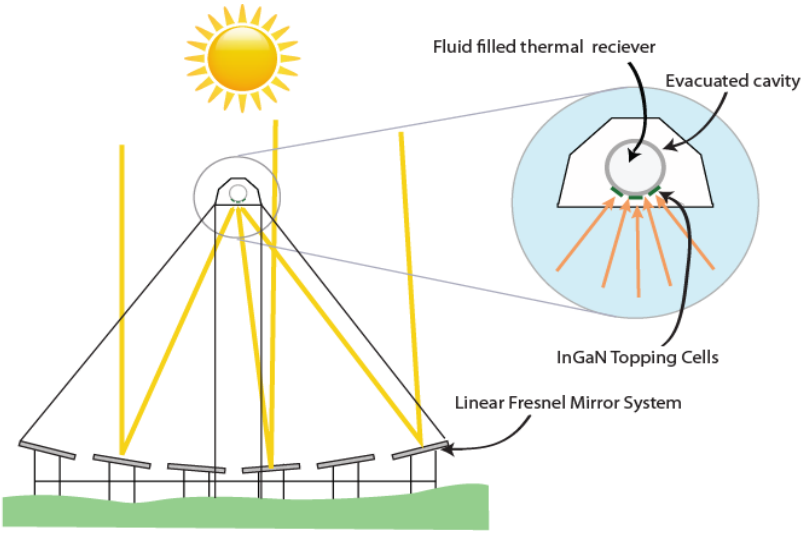

Figure 1.1 Schematic of the CSP hybrid system, showing the topping cell integrated onto the thermal receiver.

crucial difference is that solar thermal technology utilizes clean solar energy and little pollution emission is produced within the whole process. On the other hand, PV is a direct process of converting sunlight into electricity. The absorption of solar light generates pairs of electrons and holes. These higher energy electrons move into an external circuit, produce both current and voltage, generating electric power. However, one shortcoming of PV systems is that semiconductor material system can only be able to absorb the spectrum with optical energy larger than its bandgap in order to excite electrons from bound valence energy state to conduction band. Thus, the red (energy smaller than semiconductor bandgap) portion of the solar spectrum will be wasted. The combination of both CSP and PV systems offer a promising approach for higher efficiency and low-cost dispatchable electricity [2]. In a hybrid concentrating solar thermal/photovoltaic system, the PV solar cell is mounted

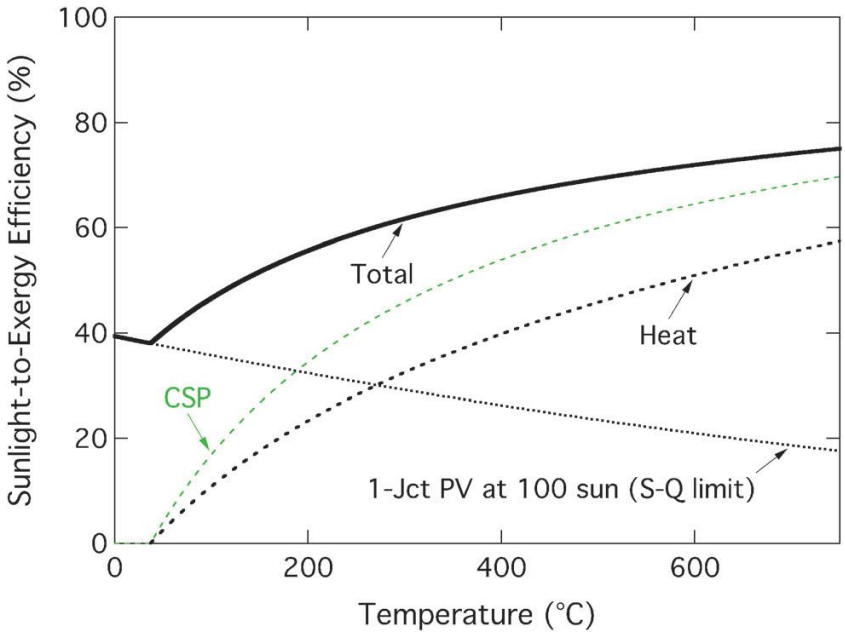

Figure 1.2 Theoretical exergy (black, solid line) efficiency limit of a 1-junction PV topping hybrid solar thermal system versus PV operational temperature at 100X concentration. There are no optical or thermal losses. PV efficiency (black, dotted line) is the thermodynamic limit for 1-junction PV with Eg free to vary. Dashed curves compare the heat exergy output without PV (green, dashed line) and in the hybrid system (black, dashed line). [2]

on top of the receiver of the CSP collector as showed in Figure 1.1. The PV cell can utilize the 'blue' portion of the solar spectrum with photon energies larger than its bandgap with higher efficiency than CSP itself regarding this corresponding part of spectrum. On the other hand, CSP systems may utilize the filtered spectrum for electricity generation. Thus, the hybrid system can use the complete solar spectrum and results in higher overall system efficiency. Figure 1.2 [2], depicts the theoretical ideal efficiency as a function of the PV operational temperature for the total hybrid converter, CSP system (without PV), heat system (CSP with PV) and Shockley-Queisser (S-Q) thermodynamic limit of 1J PV under

100 suns, respectively. The total hybrid system energy efficiency, η_x, of the ideal PV topping system is

$$\eta_x = \eta_{PV} + (1 - \eta_{PV})\left(1 - \frac{T_c}{T_h}\right) \quad (1.1)$$

This equation is based on the electrical efficiency that would be achieved via an ideal Carnot engine converting the heat to electricity with its cold side at T_c, and its hot side, T_h (temperature of the hot PV). η_{PV} is the hot PV cell (S-Q) thermodynamic limit efficiency at T_h. For the thermal dynamic efficiency calculation, 100 Suns of AM1.5D illumination has been used. In general, the PV cell efficiency (black, dotted line) decreases with temperature, especially due to the degradation of V_{oc}. T_c is assumed to be 37 °C which is the typical temperature of power plant cooling systems. The dashed black line shows the efficiency solely from the storable heat in the hybrid system. On the other hand, the dashed green line shows the efficiency from CSP system without the PV topping cell whose energy efficiency is obviously larger than the former case due to unfiltered spectrum (with no PV absorption). It results in the total efficiency that firstly decreases with temperature below 37 °C, which is dominated by PV cell then starts to increase due to the energy efficiency increment of CSP system under high temperatures. Figure 1.2 demonstrates that a high operational temperature for the PV cell is required to realize a high energy efficiency hybrid solar thermal system.

Although predicted to have high efficiency [2], [3], this hybrid system fails in practice because conventional PV cells (Si and GaAs) cease to operate at high temperatures, whereas concentrating solar thermal converter lose efficiency at low temperatures. In that regard, the InGaN material system provides a platform for high temperature PV solar cells, since nitride based electronics have already been demonstrated to operate at high

temperatures (>400 °C) [4]–[7]. Besides application as hybrid thermal converters, high temperature InGaN solar cells are also applicable for scientific space missions, for example, the 465 °C PV devices are required for instrumenting the Venus surface probe mission.

1.2 InGaN/GaN Material Properties

Besides the system thermal stability mentioned above, InGaN also has a tunable bandgap, which varies from 0.65 to 3.42 eV [8]. It can cover a broad solar spectrum from the near-infrared to the near-ultraviolet wavelength region. The temperature dependence of the direct band gap of InGaN can be described by the following equation

$$E_g(T) = E_g(300) - Eg_\alpha \left(\frac{300^2}{300+Eg_\beta} - \frac{T^2}{T+Eg_\beta}\right) \quad (1.2)$$

Then, the $In_xGa_{1-x}N$ bandgap versus Indium mole fraction at any temperature can be obtained at any temperature by interpolation including bowing for InN and GaN, which is described as :

$$E_{g_{In_xGa_{1-x}N}}(x,T) = xE_{g_{InN}}(x,T) + (1-x)E_{g_{GaN}}(x,T) - x(1-x)b \quad (1.3)$$

where b represents the bowing parameter. Parameters for the temperature and Indium mole fraction dependent $In_xGa_{1-x}N$ bandgap calculation are summarized in Table 1.

TABLE I
GaN/InGaN Bandgap Parameters

Property	GaN	InN
Eg(300) (eV)	3.42[9]	0.65[10]
Eg_α (meV/K)	0.909[9]	0.414[10]
Eg_β (K)	830[9]	454[10]
b	1.43[11]	1.43[11]

Due to the direct bandgap of the InGaN material system, InGaN has demonstrated a high absorption coefficient, which makes it suitable for PV applications. The extinction

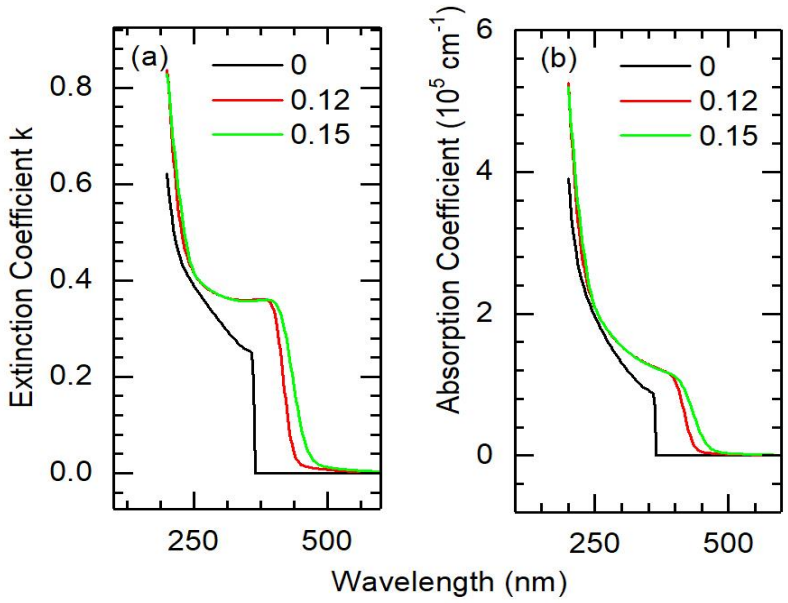

Figure 1.3 (a) InGaN extinction coefficient measured by ellipsometry technique and the corresponding. Courtesy of Dr. Alec Fisher from ASU. (b) absorption coefficient for Indium mole fraction 0 (GaN), 0.12 and 0.15.

coefficient k of GaN, $In_{0.12}Ga_{0.88}N$ and $In_{0.15}Ga_{0.85}N$ are measured by ellipsometry techniques (Figure 1.3). Then absorption coefficient α can be derived through

$$\alpha = \frac{4\pi}{\lambda} k \tag{1.4}$$

where λ is wavelength of the spectrum, for optical generation calculation. For other indium mole fractions, the InGaN optical constants are obtained by shifting the spectrum with the corresponding bandgap difference. The absorption coefficient of InGaN near the bandgap edge are in the order of ~10^5 cm^{-1}. A high absorption coefficient means a thinner InGaN absorber is needed during device fabrication, which could reduce the cost of nitride PV cells. In addition, the collection of reliable mobility properties are also required for proper

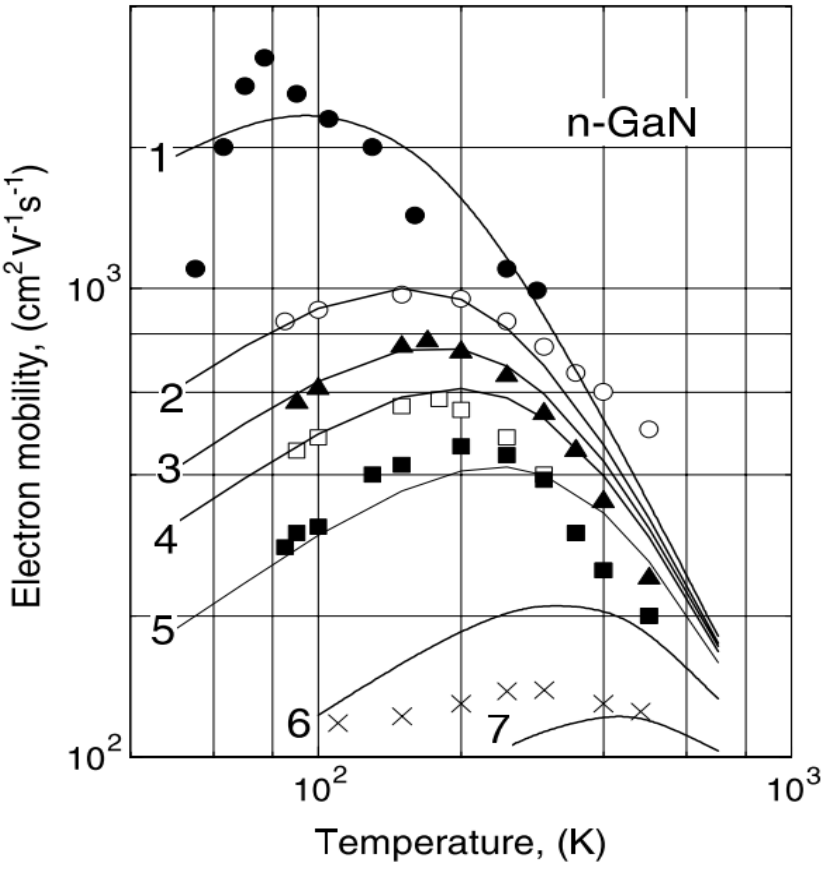

Figure 1.4 Temperature and doping concentration dependent model of GaN mobility model developed by by T. Mnatsakanov et al. [12]. Curves represent the best approximation according to Equation 1.3 and 1.4 and parameter values listed in Table 2: 1--$N = 3 \times 10^{16}\ cm^{-3}$, 2--$N = 10^{17}\ cm^{-3}$, 3--$N = 1.5 \times 10^{17}\ cm^{-3}$, 4--$N = 2 \times 10^{17}\ cm^{-3}$, 5--$N = 3.5 \times 10^{17}\ cm^{-3}$, 6--$N = 10^{18}\ cm^{-3}$, 7--$N = 3 \times 10^{18}\ cm^{-3}$.

device simulation. An electron mobility model as a function of carrier concentration and temperature has been developed by Mnatsakanov et al. [12] based on the experimental mobility data. This model has been adopted for nitride materials in this simulation work:

$$\mu_n(N,T) = \mu_{max,n}(T_0)\frac{B_n(N)\left(\frac{T}{T_0}\right)^{\beta_n}}{1+B_n(N)\left(\frac{T}{T_0}\right)^{\alpha_n+\beta_n}} \tag{1.5}$$

where T_0 = 300 K and

$$B_n(N) = \left[\frac{\mu_{min,n} + \mu_{max,n}\left(\frac{N_{g,n}}{N}\right)^{\gamma n}}{\mu_{max,n} - \mu_{min,n}}\right]\Big|_{T=T_0} \tag{1.6}$$

This model is derived from the well-known Caughey-Thomas mobility approximation [13] at room temperature:

$$\mu_i(N, 300) = \mu_{min,i}(300) + \frac{\mu_{max,i}(300) - \mu_{min,i}(300)}{1 + \left(\frac{N}{N_{g,i}}\right)^{\gamma_i}} \tag{1.7}$$

where i = n, p for electrons and holes respectively, N is the doping concentration, and the model parameter $\mu_{max,i}(300)$, $\mu_{min,i}(300)$, $N_{g,i}$ and γ_i depend on the type of semiconductor material. As shown in Figure 1.4, at low temperatures, Coulomb scattering dominates the mobility and the mobility increases with temperature. In contrast, at high temperature, the main contribution is phonon scattering, mobility decreases with increasing temperatures.

For holes, the parameters for the Caughey-Thomas mobility model at room temperature have also been reported by Mnatsakanov et al. [12] as shown in Figure 1.5(a). However, due to the lack of experimental data of various temperatures under different acceptor concentrations, only optical phonon scattering is considered at high temperature for simplification in this work as shown in Figure 5(b),

$$\mu_p(N, T) = \mu_p(N, 300)\left(\frac{T}{300}\right)^{-\alpha_p} \tag{1.8}$$

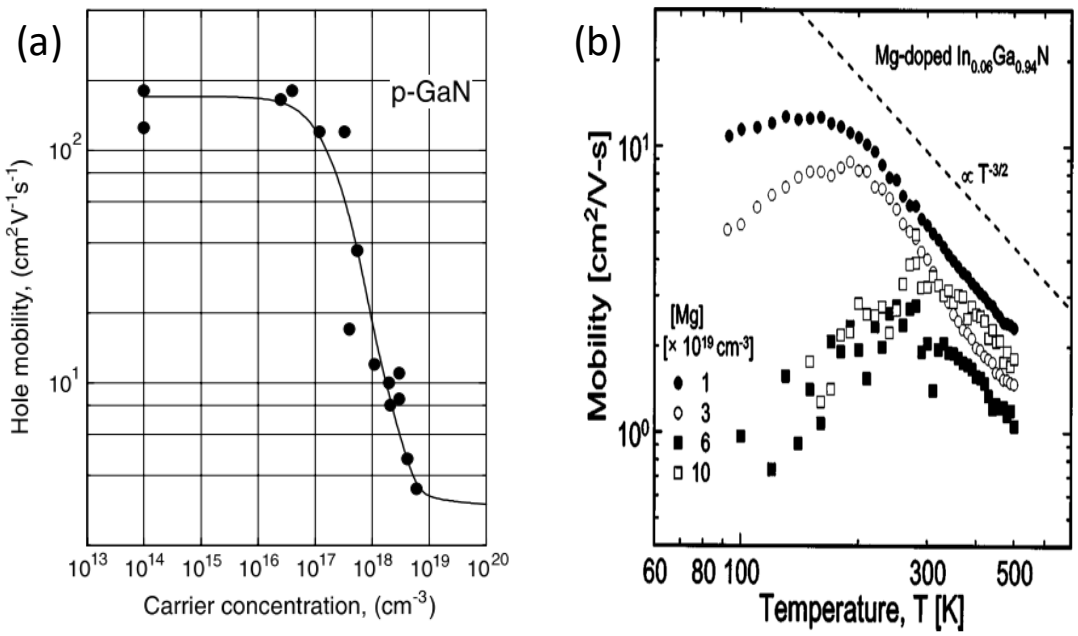

Figure 1.5: (a) Low field hole mobility as a function of doping concentration in wurtzite GaN at room temperature [12]. (b) Temperature dependences of Mg-doped $In_{0.06}Ga_{0.94}N$ hole mobility with varying doping concentration from 1×10^{19} to $1 \times 10^{20}\ cm^{-3}$ [14]

TABLE II
Material Parameters used for mobility models [12][14]

Property	GaN	InN
$\mu_{min,n}(300)$	55	55
$\mu_{min,p}(300)$	3	3
$\mu_{max,n}(300)$	1000	1000
$\mu_{max,p}(300)$	170	170
$N_{g,n}$	2×10^{17}	2×10^{17}
$N_{g,p}$	3×10^{17}	3×10^{17}
α_n	2.0	2.0
α_p	1.5	1.5
γ_n	1.0	1.0
γ_h	2.0	2.0
β_n	0.7	0.7

where α_p = 1.5 [14]. Thus, temperature and doping dependent mobility models as

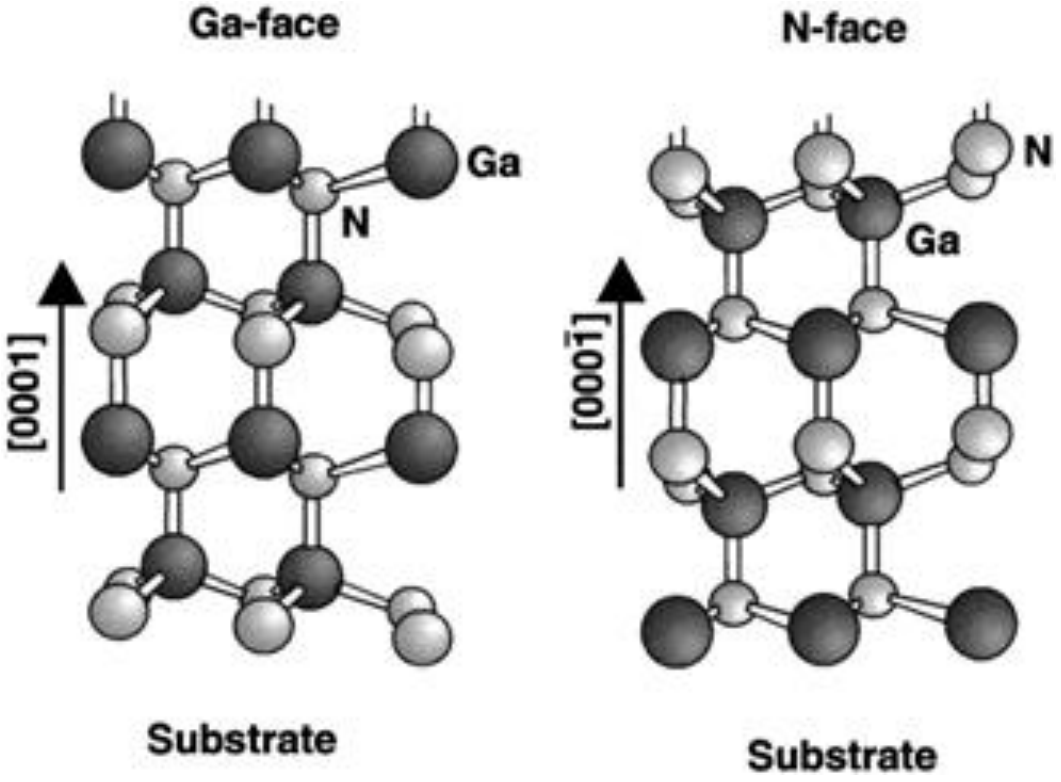

Figure 1.6: Ga-faced and N-faced wurzite GaN structure.

summarized in Table 2 for electrons and holes have been developed for further solar device simulation.

Polarization effects between GaN and InGaN hetero-interface are also an important material property for electronic devices based on nitride material. The total macroscopic polarization charge in GaN, InGaN or AlGaN consists of the spontaneous polarization charge, P_{SP}, of the equilibrium lattice and strain induced piezoelectric polarization charge , P_{PE}. The spontaneous polarization charge in an intrinsic property related to the bonding nature of the material. Its origin can be ultimately attributed to the fact that the geometric center of the positive charges (nuclei) in the solid does not coincide with the center of the negative charges (electrons) in non-cubic wurztie material. Most common semiconductors

are cubic and hence these coincide and there is no spontaneous polarization as occurs in the InGaN system. Tetrahedrally coordinated semiconductors with cubic structure have four equivalent sp^3 hybridization bonds. However, as a wurtzite structure, III-Nitride material have a lower symmetry crystal and the split-off of the valence band top at Γ into a single and double degenerate band shows the existence of an asymmetry in the bonding. This intuitive explanation of the origin of P_{SP} shows why elemental semiconductors such as Si, C, Ge and zincblende-structure materials such as most of III-V and II-IV semiconductors, do not have spontaneous polarization properties. When applying strain to the crystal structure, the symmetry of the bonds is further changed and piezoelectric polarization is induced.

Nitride compounds exhibit two different sequences of atomic layering: $[0001]$ and $[000\bar{1}]$. In the case of GaN layers, heteroepitaxial layers are either Ga- faced or N- faced. For Ga-face structures, the Ga layer is on the top of surface of the {0001} basal plane. It is important to note that the $[0001]$ and $[000\bar{1}]$ grown GaN have very different physical and chemical properties [15]. Figure 1.6 depicts the crystal structure of wurtzite Ga-faced and N-face GaN, separately. Ga-face and N-face nitride materials have opposite polarization effect at the hetero-interface, as shown in Figure 1.7 [16]. Typically, the electric field originating from the p-n junction of a solar cell separates and drifts photo-carriers to the electrodes for collection. It can be observed from Figure 1.7(a) that, for the conventional Ga-face configuration, the direction of the polarization-induced electric field is opposite to

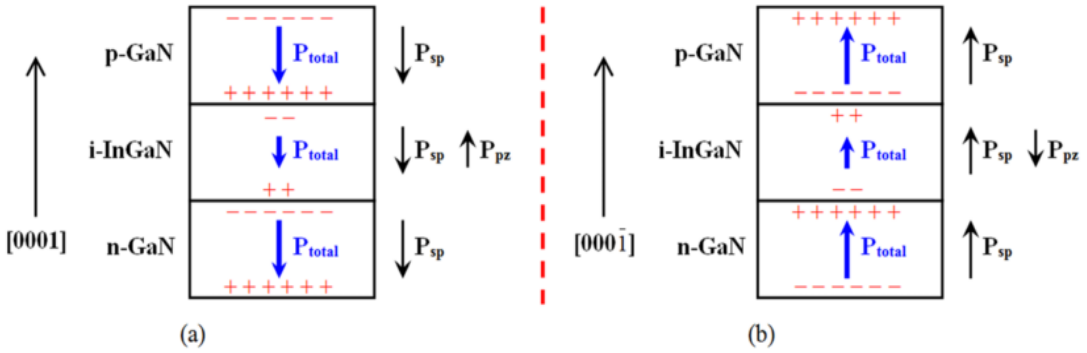

Figure 1.7: Spontaneous (P_{SP}) and Piezoelecric (P_{PE}) Polarization schematic diagrams of Ga-face (a) and N-face (b) p-on-n GaN/InGaN structure [16].

built-in filed from the junction, and thus will degrade carrier collection of the cell. In contrast, for N-face configuration, the polarization induced field is reversed and aligned with the built-in electric field, which will be beneficial for carrier collection. However, in practice, (0001) orientation with Ga-face polarization is the conventional material growth direction for InGaN solar cells. Band engineering technique has been investigated for performance improvement in the following chapters.

Since conventional GaN devices are grown with Ga-face material, the calculation of polarization charge in Ga-faceGaN/InGaN p-on-n devices is illustrated below. Total polarization P_t is characterized by two components,

$$\mathrm{P}_t = \mathrm{P}_{sp} + \mathrm{P}_{pz} \tag{1.9}$$

where P_{sp} is constant determined by material's intrinsic property. The piezoelectric polarization, P_{pz}, is given by:

$$P_{PZ} = 2\frac{a_s - a_0}{a_0}\left(e_{31} - \frac{c_{13}}{c_{33}}e_{33}\right) \tag{1.10}$$

TABLE II
Material Parameters used for polarization models [34]

Property	GaN	InN	Unit
P_{sp}	-0.034	-0.042	C/m^2
e_{31}	-0.34	-0.41	C/m^2
e_{33}	0.67	0.81	C/m^2
c_{13}	100	92	GPa
c_{33}	392	224	GPa
a_0	3.189	3.548	Å

where E_{31} and E_{33} are piezoelectric constants, and C_{13} and C_{33} are elastic constants. a_s and a_0 are the lattice constants of the substrate and the epi-layer, respectively. The net charge σ at a specific hetero-interface is given by:

$$\sigma = \mathrm{P(Top)} - \mathrm{P(Bottom)} \tag{1.11}$$

$$\sigma = [\mathrm{P_{SP}(Top)} + \mathrm{P_{PE}(Top)}] - [\mathrm{P_{SP}(Bottom)} + \mathrm{P_{PE}(Bottom)}] \tag{1.12}$$

All the parameters for polarization calculation has been summarized in Table 2. Due to the screening effect of free carriers on polarization, there are difference between the theoretical and experimental values for polarization in the hetero-interface. The screening factor is assumed to be 0.4 which is taken from previous studies [8].

1.3 A State-of-art Review of InGaN Photovoltaics

Since InGaN has demonstrated promising material properties for PV applications, research interest in InGaN/GaN solar cells has been increasing in the past decade. Various configurations of InGaN PV devices have been studied extensively, such as InGaN homo-junctions, InGaN/GaN hetero-junctions, p-n, p-i-n and Multiple Quantum Well (MQW) type devices. Devices have been grown by MBE or MOCVD technology, demonstrating various base InGaN bandgaps with Indium mole fraction ranging from ~2% up to ~54% [17], [18]. The InN bandgap was originally thought to be ~ 1.9 eV [19] among the nitride

research community. Later on, the researchers found that the presence of oxygen contamination caused this confusion[20]. Bandgap of InN then has since been revised down to 0.65 eV at room temperature [21]–[23]. Thus, the revised tunable bandgap of InGaN could respond to almost the whole solar spectrum. In that regard, researchers' interest has been increasing on its possible application in the PV area. InGaN solar devices with 2.4V high V_{oc} but very low J_{sc} were fabricated in 2007 by Jani et al. with a p-i-n mesa configuration[24]. Then Neufeld et al. demonstrated an improved device with an indium mole faction 0.12 in 2008. The performance of the fabricated $In_{0.12}Ga_{0.88}N$ single junction p-i-n cell has demonstrated a J_{sc} of 4.2 mA/cm^2, V_{oc} of 1.81 V, and a FF of 0.75 under concentrated AM0 spectrum. MQW devices have been introduced for InGaN p-i-n mesa configurations since InGaN well absorber layers can maintain better material quality as they are strained in each MQW period. The growth of high indium mole fraction (~0.35) InGaN cell has been realized by Dahal et al. in 2010 based with a MQW configuration[25]. A 12 period of MQW device with 3 nm $In_{0.35}Ga_{0.65}N$ as well material and 17 nm GaN as barrier material has been demonstrated. At room temperature and under AM 1.5 irradiation, it generated a cell performance with Jsc of 2.56 mA/cm^2, Voc of 1.80 V, FF of 0.64 and energy conversion efficiency 2.95 %. The MQW structure generates higher Jsc, which is attributed to a better absorber material quality with less defects and non-radiative recombination centers. The highest solar performance results with 5.95% photovoltaic efficiency has been reported to date was by Liou et al[26]. They have reported an InGaN MQW device based on a SiCN/Si(1 1 1) substrate. The proposed and fabricated devices with indium mole fraction of 0.19 to 0.36, have demonstrated impressive solar performance with a low dark current density (J_d) of 2.14 to 8.88 $\mu A/cm^2$, a high J_{sc} of 2.72 to 2.97

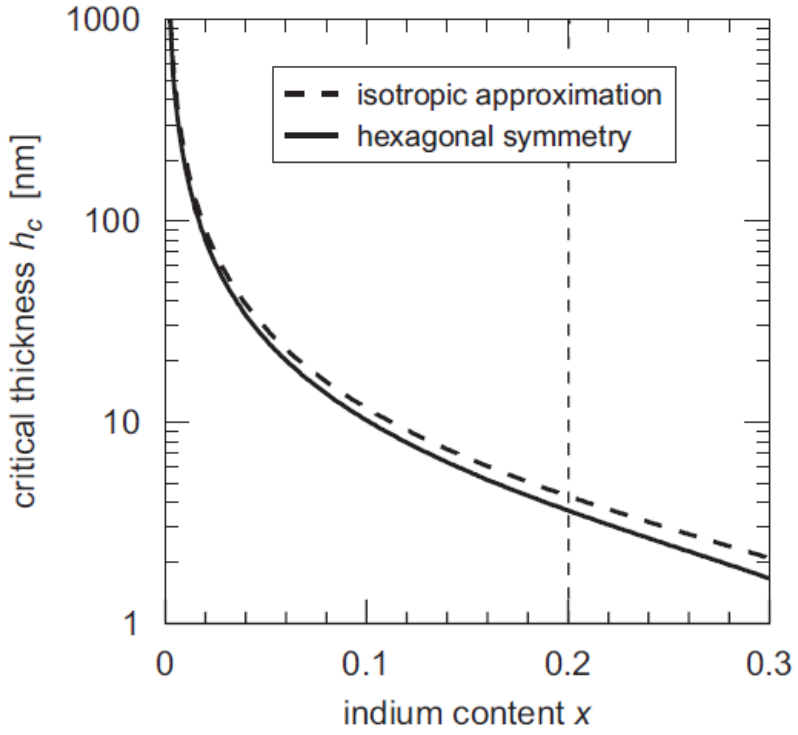

Figure 1.8: Critical thickness of $In_xGa_{1-x}N$ on top of GaN substrate as a function of indium mole fraction under isotropic approximation and hexagonal symmetry model[27].

mA/cm^2, a high Voc of 2.72 to 2.92 V, a high FF of 0.61 to 0.74. Thus, since the beginning periods of InGaN PV cell research and development, the nitride solar cell research community has been significantly improving the upper limit of InGaN PV efficiency. However, there is still a huge gap between the performance achieved to date and the expectation for final commercial application. The poor performance of fabricated device has been limited by a lot of roadblocks such as low indium mole fraction, poor crystalline quality and phase separation of the fabricated InGaN absorber. Large lattice mismatch between GaN and InN, makes low bandgap InGaN growth very difficult. The critical

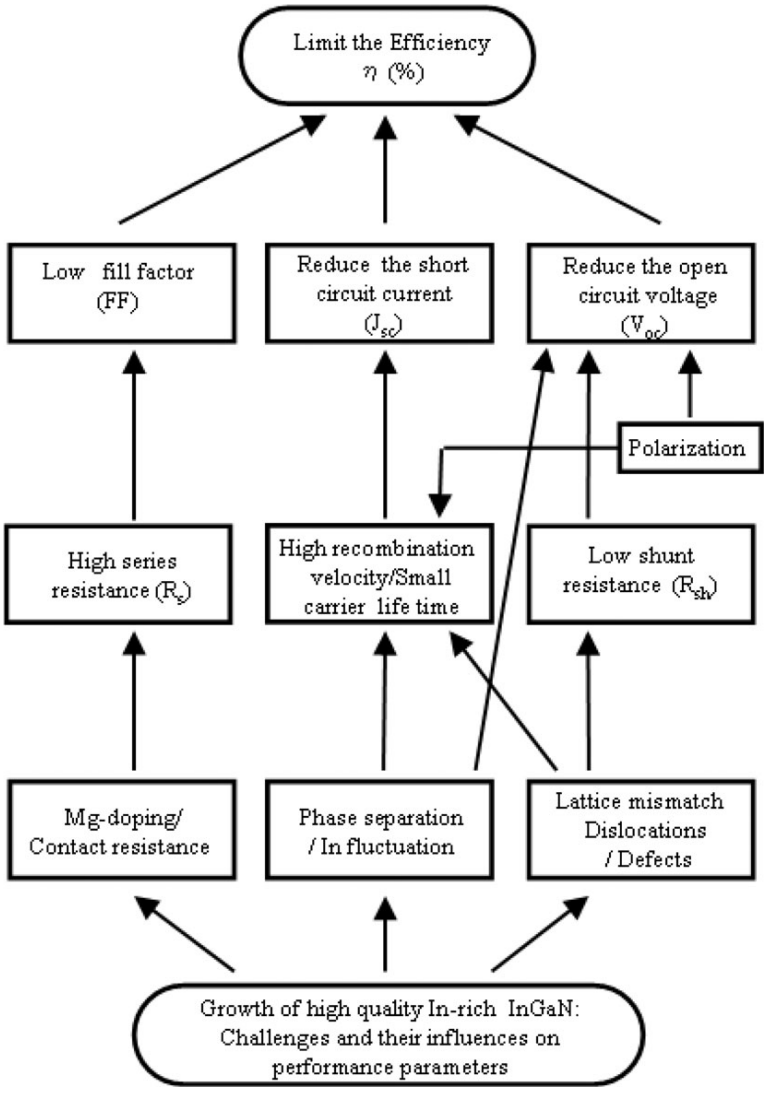

Figure 1.9: Schematic of material fabrication challenges and their impact on performance parameter degradation of InGaN solar cell[33].

thickness of InGaN grown on top of GaN substrate decreases rapidly for larger mole fraction as shown in Figure 1.8[27]. Beyond the critical thickness, the strain energy is relaxed with the formation of dislocation and defects. The lack of high enough quality thick InGaN film results in transmission loss for photons with energy higher than the absorber bandgap and recombination loss for generated photo-carriers. Phase separation in the

InGaN alloy due to the miscibility gap between InN and GaN, is another challenge for high performance InGaN solar cell[28]. The phase separation domains could act as recombination centers, decreasing J_{sc} and V_{oc} of the solar cell. The indium content fluctuation in InGaN for MQW device can also play negative effects on its solar performance as reported by Lai et al.[29]. What is more important, p-type conductivity is necessary for PV cell, but, very challenging to achieve for InGaN and GaN. First, a high background n-type doping from defects compensates the hole's concentrations [30]. Moreover, the deep activation level of Mg in p-type is around 204 meV [31] and leads to high incomplete ionization resulting in low hole concentrations at room temperature. Besides the material quality challenges, the spontaneous and piezoelectric polarization inherent in the wurzite nitrides may introduce spikes in the band diagram due to the combination of the band offset and polarization at the InGaN/GaN interface, which may lead to suppression of the photo-generated carriers [32]. The material property roadblocks and their impact on performance parameter degradation of InGaN solar cell have been nicely summarized by Bhuiyan et al. [33] in a review paper as shown in Figure 1.9.

Despite these challenges, the present work proposes a path to high efficiency InGaN 2J tandem solar cells operating at high temperature via numerical simulation. In Chapter 2, a 1J InGaN solar cells have been simulated at 450 ℃. Polarization and band offset effects in the solar cell performance have been investigated. Band engineering technology has been adopted to suppress polarization effects to achieve better photo-carriers collection. Moreover, the base doping and thickness have been optimized for optimum solar efficiency. The SRH lifetime and solar concentration impact on the optimized device demonstrates long SRH lifetime and larger concentration can compensate the V_{oc} reduction

at high temperatures. In Chapter 3, a polarization engineered GaN/InGaN tunnel diode with a p-i-n configuration has been adopted for improved tunneling current. With the optimized 1J cell and tunneling diode for a series connection, a high efficiency tandem cell has been designed working under high temperature and solar concentrations. Besides monolithic multiple junction solar cell designs, mechanical multiple junction solar cell configurations for InGaN cells have been investigated, and a novel configuration for multiple junction cells with the same bandgaps connected via tunnel junctions has been proposed to bypass the grown challenge for thick InGaN film. In Chapter 4, AR-Coatings have been designed to reduce the front reflection loss in InGaN PV cell for optical management. Finally, in Chapter 5, an effective mobility model for InGaN MQW well devices has been developed for faster numerical simulation of quantum devices in classical device simulator such as Silvaco Atlas.

CHAPTER 2

1J SOLAR CELL SIMULATION

2.1 Commercial TCAD Package: Silvaco Atlas

Most work in this dissertation uses Silvaco Atlas [34] to perform solar cell simulation. Atlas is a commercial TCAD (Technology Computer Aided Design) package that provides DC, AC, and transient modeling for semiconductor devices. Electrical, thermal and optical simulation for two- and three-dimensional devices are provided for predictive parametric analysis of novel device structures. This virtual semiconductor process and design tool obviously can help increase with development speed and reduce

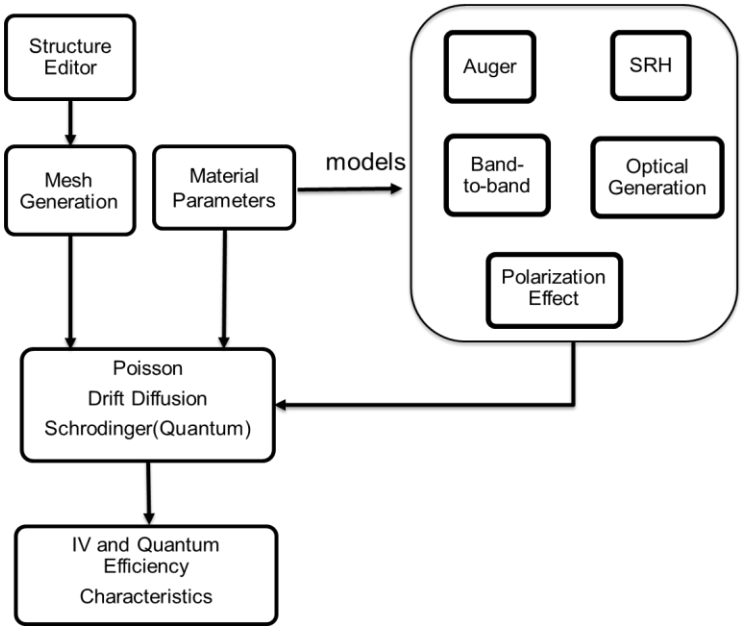

Figure 2.1 Flow diagram of the simulation model for MQW solar cell in ATLAS.

risks and uncertainties. Figure 2.1 shows a flow-chart of the InGaN/GaN solar cell device modeling in Silvaco ATLAS. First, the device structure is generated and meshed for finite element simulation. Second, the necessary material parameters are collected from literature

and measurement as input for models such as recombination (Auger, SRH and Band-to-band recombination), optical generation and polarization effects. The Poisson, drift-diffusion and Schrödinger equations are coupled and solved for the I-V and quantum efficiency (QE) characteristics of the device. Either raytracing or the Transfer Matrix Method (TMM) may be used for optical generation.

2.2 Drift Diffusion Model

The Drift-Diffusion model is used for carrier transport in bulk material solar cell simulation. The model solves the Poisson and electron-hole continuity equations self consistently:

$$\nabla\big(\varepsilon(\nabla\phi)\big) = -q(p - n + N_D^+ - N_A^-) \tag{2.1}$$

$$\frac{\partial n}{\partial t} = \frac{1}{q}\nabla \cdot J_n - R + G \tag{2.2}$$

$$\frac{\partial p}{\partial t} = -\frac{1}{q}\nabla \cdot J_p - R + G \tag{2.3}$$

where ε is the dielectric function, q is the elementary charge, ϕ is the electrostatic potential, n and p are the electron and hole densities, N_D^+ and N_A^- are the concentrations of ionized donors and acceptors, R and G are the recombination and generation rates, J_n and J_p are the current densities of electrons and holes. These equations can be solved self-consistently with Gummel's iteration scheme [35], [36].

First, the equilibrium nonlinear Poisson equation can be solved based on the following quasi-linearization procedure. First rewrite the 1-D Poisson equation (Equation 2.1) into the form

$$\frac{d^2\phi}{dx^2} = -\frac{qn_i}{\varepsilon}\left(e^{-\frac{\phi}{V_T}} - e^{-\frac{\phi}{V_T}} + C\right) \tag{2.4}$$

with n, p, and C from Equation 2.1 being defined as following:

$$n = n_i e^{\frac{\phi}{V_T}} \tag{2.5}$$

$$p = n_i e^{\frac{\phi}{-V_T}} \tag{2.6}$$

$$C = (N_D^+ - N_A^-)/n_i \tag{2.7}$$

where n_i is the intrinsic carrier concentration and $V_T = kT/q$ is the thermal voltage.

Within one iteration cycle, assuming the intial potential as ϕ^{old} and new potential value for next iteration cycle as ϕ^{new}. Substitute $\phi^{new} = \phi^{old} + \delta$ into Equation 2.4 with linearization $\exp(\pm\delta/V_T) \approx 1 \pm \delta/V_T$, and one obtains

$$\frac{d^2\phi^{new}}{dx^2} - \frac{qn_i}{\varepsilon V_T}\left(e^{-\frac{\phi^{old}}{V_T}} + e^{\frac{\phi^{old}}{V_T}}\right)\phi^{new} = -\frac{qn_i}{\varepsilon}\left(e^{-\frac{\phi^{old}}{V_T}} - e^{\frac{\phi^{old}}{V_T}} + C\right) - \frac{qn_i}{\varepsilon V_T}\left(e^{-\frac{\phi^{old}}{V_T}} + e^{\frac{\phi^{old}}{V_T}}\right)\phi^{old} \tag{2.8}$$

Rewriting the above equation in terms of the carrier concentrations p and n with Equation 2.5 and 2.6, one obtains

$$\frac{d^2\phi^{new}}{dx^2} - \frac{q}{\varepsilon V_T}(p+n)\phi^{new} = -\frac{q}{\varepsilon}(p - n + C) - \frac{q}{\varepsilon V_T}(p+n)\phi^{old} \tag{2.9}$$

Now via finite difference discretization and assuming a uniform mesh for simplicity, one can obtains:

$$\frac{d^2\phi_i}{dx^2} \approx \frac{\phi_{i+1} - 2\phi_i + \phi_{i-1}}{\Delta^2} \tag{2.10}$$

where i labels the grid element and Δ is the meshing size.

Substituting Equation 2.10, and normalizing Δ with the intrinsic Debye length, L_D, and ϕ_i with V_T, Equation 2.9 can be rewritten as:

$$\frac{1}{\Delta^2}\phi_{i+1}^{n+1} - \left(\frac{2}{\Delta^2} + p_i + n_i\right)\phi_i^{n+1} + \frac{1}{\Delta^2}\phi_{i-1}^{n+1} = -(p_i + n_i + C_i) - (p_i + n_i)\phi_i^n \tag{2.11}$$

where n denotes the iteration number.

Equation 2.11 then can be rewritten in the matrix form as:

$$[\mathrm{A}][\phi] = [F] \tag{2.12}$$

where F is the forcing function and actually is the RHS of Equation 2.11. Matrix A is diagonally dominant and can be solved via LU decomposition method with stable convergence.

Besides the Poisson equation, the carrier continuity equations can be discretized via the Scharfetter- Gummel method. The discretization of the continuity equations requires the value of the currents on the midpoints for two neighboring grid nodes. Interpolation schemes are needed to determine the midpoint currents. One can assume the potential varies linearly between two neighboring nodes, which is consistent with the assumption that the electric field is constant between two neighboring nodes. For the carrier density, one might assume a similar linear variation by intuition. However, this simple approach is only reliable for a very small potential variation between the nodes. It leads to the field between the two nodes being zero which implies the same carrier density on two neighboring nodes.

Scharfetter and Gummel provide an optimal solution to this problem. They proposed that the carrier density follows an exponential variation between two neighboring mesh points:

$$\mathrm{n(x)} = [1 - \mathrm{g(x}, \phi)]\mathrm{n}_i + \mathrm{g(x}, \phi)\mathrm{n}_{i+1} \tag{2.13}$$

where $\mathrm{g(x}, \phi)$ is the growth function

$$\mathrm{g(x}, \phi) = \frac{[1-\exp((\phi_{i+1}-\phi_i)(x-x_i))]}{1-\exp((\phi_{i+1}-\phi_i))} \tag{2.14}$$

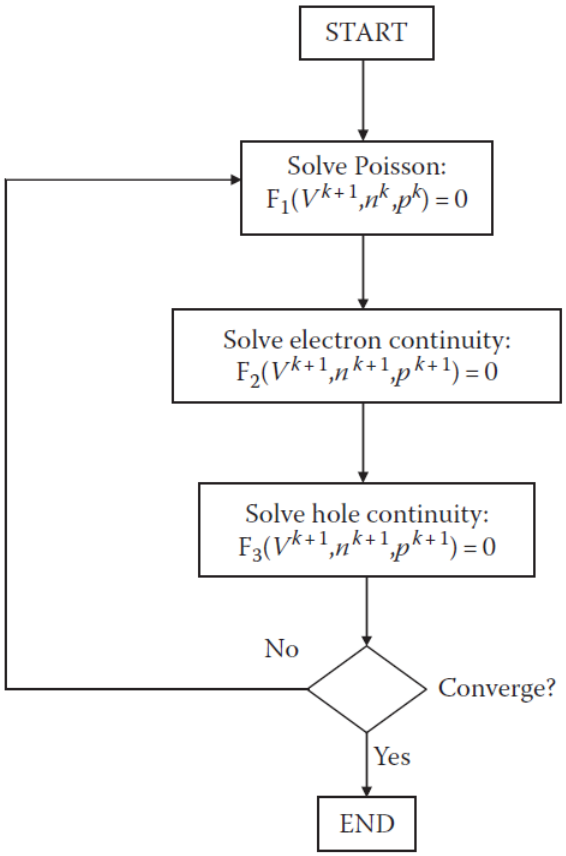

Figure 2.2 Gummel's iteration scheme for the drift-diffusion model[36]

where x is the normalized position between mesh element i and element $i+1$ and potential ϕ on the corresponding mesh element is also normalized.

Current equations for electrons and holes are given by:

$$J_n = qn\mu_n E + qD_n \nabla \mathrm{n} \tag{2.15}$$

$$J_p = qp\mu_p E - qD_p \nabla \mathrm{p} \tag{2.16}$$

The final form of the discretized electron current equation (Equation 2.15) is given by

$$J^n_{i-1/2} = \frac{qD^n_{i-1/2}}{\Delta}[\mathrm{n}_i B(\phi_i - \phi_{i-1}) - \mathrm{n}_{i-1} B(\phi_{i-1} - \phi_i)] \tag{2.17}$$

where

$$B(x) = \frac{x}{e^x - 1} \tag{2.18}$$

is the Bernoulli function. Assuming steady state conditions ($\frac{\partial n}{\partial t} = 0$), substitute Equation 2.17 into Equation 2.2, to obtain:

$$\frac{D^n_{i-1/2}}{\Delta^2} B(\phi_{i-1} - \phi_i) \mathrm{n}_{i-1} - \left[\frac{D^n_{i+\frac{1}{2}}}{\Delta^2} B(\phi_i - \phi_{i+1}) + \frac{D^n_{i-\frac{1}{2}}}{\Delta^2} B(\phi_i - \phi_{i-1}) \right] \mathrm{n}_i + \frac{D^n_{i+\frac{1}{2}}}{\Delta^2} B(\phi_{i+1} -$$

$$\phi_i) \mathrm{n}_{i+1} = R_i - G_i \tag{2.19}$$

Similarly, for holes, one can get

$$\frac{D^n_{i-1/2}}{\Delta^2} B(\phi_i - \phi_{i-1}) \mathrm{p}_{i-1} - \left[\frac{D^n_{i+\frac{1}{2}}}{\Delta^2} B(\phi_{i+1} - \phi_i) + \frac{D^n_{i-\frac{1}{2}}}{\Delta^2} B(\phi_{i-1} - \phi_i) \right] \mathrm{p}_i + \frac{D^n_{i+\frac{1}{2}}}{\Delta^2} B(\phi_i -$$

$$\phi_{i+1}) \mathrm{p}_{i+1} = R_i - G_i \tag{2.20}$$

Then the discretized continuity equations (Equation 2.19 and Equation 2.20) together with the linearized and discretized Poisson equation (Equation 2.11) are solved self-consistently for the semiconductor device performance, especially I-V curves via Gummel's iteration method.

As shown in Figure 2.2, Gummel's method solves the coupled set of Poisson and the carrier continuity equations via a decoupled procedure. First, the potential is obtained from the linearized Poisson's equation. The potential then is substituted into the continuity equations. The solution will be substituted back into Poisson's equation given by Equation 2.11. The whole process is repeated until convergence is reached, when the residual of the coupled equations is less than a set tolerance.

The drift-diffusion (DD) model from Silvaco Atlas has been first validated with our in-house DD solver programmed in Matlab. A simple p-$In_{0.12}Ga_{0.88}N$/n-$In_{0.12}Ga_{0.88}N$ solar device has been simulated. It consists of a 50-nm-thick, $10^{19}cm^{-3}$ p-doping $In_{0.12}Ga_{0.88}N$ top

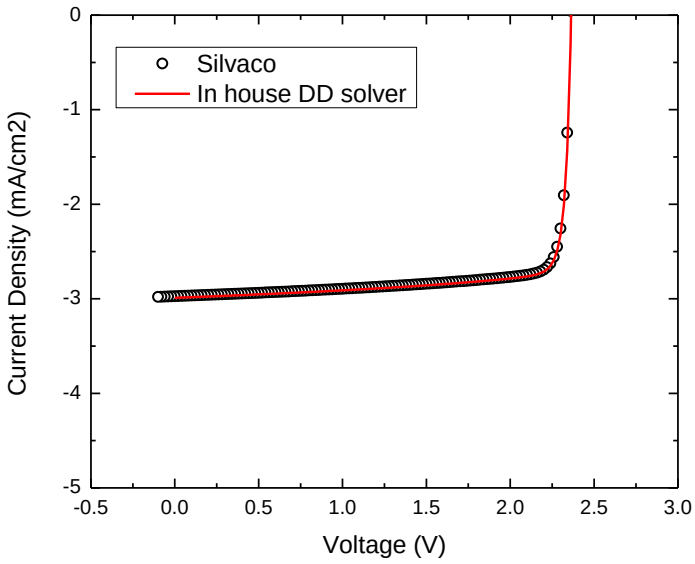

Figure 2.3 Compare between Silvaco and In house Drift-diffusion Solver for $In_{0.12}Ga_{0.88}N$ Device under room temperature.

layer and a 500-nm-thick, $10^{17}cm^{-3}$-n-doping UID-$In_xGa_{1-x}N$ base layer. In addition, the AM1.5 solar spectrum is used as a light source in the optical simulations. A 5 ns SRH lifetime for electrons and holes are assumed based on lifetime measurements. A band to band recombination coefficient of $1.1\times10^{-11}cm^3/s$ is assumed [37]. Auger recombination coefficients for the nitride materials from the literature vary from 1×10^{-34} to 5.37×10^{-28} cm^6/s [38]. A fixed value of 1×10^{-31} cm^6/s is assumed for electrons and holes of InGaN in the simulation. A front surface recombination velocity of 10^4 cm/s is used from measurement. As shown in Figure 2.3, the Silvaco results show good consistency with simulation results from our In-house DD solver, which demonstrates that Silvaco Atlas is reliable for solar cell device simulation. It was adopted here for novel device design with

more complicated physics models such as quantum tunneling, thermionic emission and polarization effect.

2.3 Detailed Balance Limit

Shockley-Queisser limit (SQ Limit) or detailed balance limit refers to the maximum theoretical efficiency of a 1J solar cell, which guided the design of InGaN solar cells in this work. This limit is the most fundamental theory in the PV field and was first calculated by William Shcokley and Hans-Joachim Queisser in 1961 [39]. The model assumes that mobility is infinite and there is complete absorption of all photons above the bandgap. The basic idea is to calculate the absorption flux from the ambient and flux emitted from the solar cell. The difference between absorption and emission corresponds to the photo-current generated from the solar cell. The total absorption is given by two parts: the absorption photon flux from the sun φ_{sun} and the absorption photon flux from the earth φ_{earth}. The absorption φ_{sun} from the sun is given by:

$$\varphi_{sun} = \frac{2\pi}{h^3c^2} Cf \int_{E_g}^{\infty} \frac{E^2}{\exp\left(\frac{E}{kT_{sun}}\right)-1} dE \tag{2.21}$$

where C is the concentration factor, solar acceptance $f = \frac{R_{sun}^2}{D_{sun}^2}$ (R_{sun} is radius of the sun and D_{sun} is distance from the sun to the earth), E_g is the bandgap and T_{sun} is the temperature of the sun. The absorption photon flux from the earth φ_{earth} is given by:

$$\varphi_{earth} = \frac{2\pi}{h^3c^2} (1 - Cf) \int_{E_g}^{\infty} \frac{E^2}{\exp\left(\frac{E}{kT}\right)-1} dE \tag{2.21}$$

The emission flux from the solar cell to ambient is given by:

$$\varphi_{emission} = \frac{2\pi}{h^3c^2} \int_{E_g}^{\infty} \frac{E^2}{\exp\left(\frac{E-qV}{kT}\right)-1} dE \tag{2.22}$$

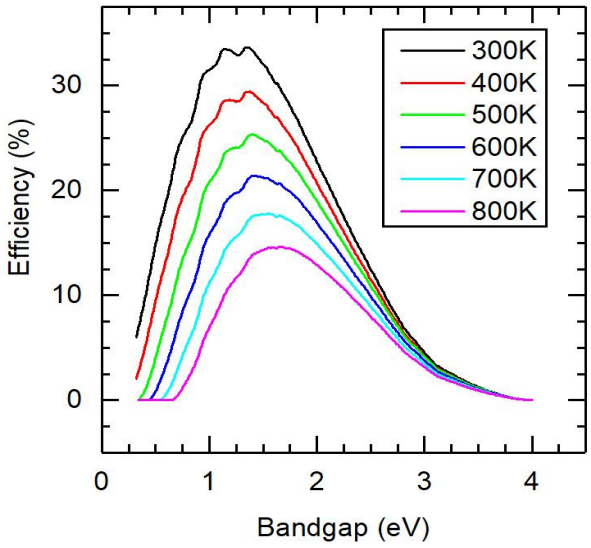

Figure 2.4 Theoretical efficiency calculated via detailed balance limit under different temperatures with 1 sun AM1.5.

Thus the J-V curve of the solar cell from detailed balance calculation may be expressed as:

$$J = q(\varphi_{sun} + \varphi_{earth} - \varphi_{emission}) = \mathrm{q} \cdot \frac{2\pi}{h^3 c^2}\left\{Cf \int_{E_g}^{\infty} \frac{E^2}{\exp\left(\frac{E}{kT_{sun}}\right)-1} dE + (1 - Cf) \int_{E_g}^{\infty} \frac{E^2}{\exp\left(\frac{E}{kT}\right)-1} dE - \int_{E_g}^{\infty} \frac{E^2}{\exp\left(\frac{E-qV}{kT}\right)-1} dE\right\} \quad (2.23)$$

where V is the voltage applied on the device.

Figure 2.4 shows the theoretical efficiency as a function of bandgap under different temperatures from 300K to 800K with increment of 100K. Obviously maximum efficiency for a given bandgap decreases with temperature. Detailed balance calculations provide a guideline for numerical device simulation through this dissertation work.

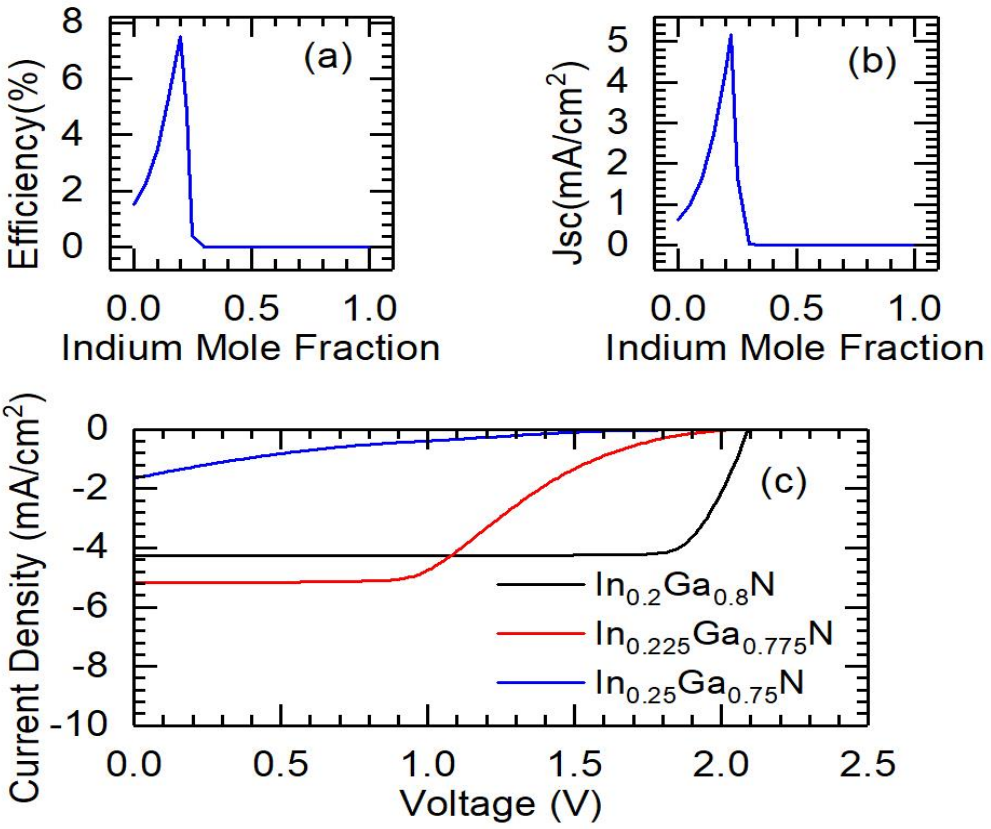

Figure 2.5 (a) and (b) Calculated conversion efficiency of a single-junction p-GaN/n-$In_xGa_{1-x}N$/n-GaN structure versus Indium composition. (c) shows IV curves of the simulated devices with $In_{0.2}Ga_{0.8}N$, $In_{0.225}Ga_{0.775}N$ and $In_{0.25}Ga_{0.75}N$, respectively.

2.4 Bandgap Engineering of a 1J InGaN Solar Cell

To understand the performance of a 2J tandem cell, we initially investigate InGaN 1J heterojunction designs at 300 K. The simulated devices consist of a 200-nm-thick, $10^{19}cm^{-3}$-doping-n-GaN bottom layer, a 500-nm-thick, $10^{17}cm^{-3}$-n-doped UID (unintentionally-doped) $In_xGa_{1-x}N$ base layer, and a 50-nm-thick, $5 \times 10^{19}cm^{-3}$-p-doping p-GaN top layer. The n-type layer is nearly ~100% ionized. Incomplete ionization has been considered for p-GaN doping in the modeling. The activation energy for Mg dopants is

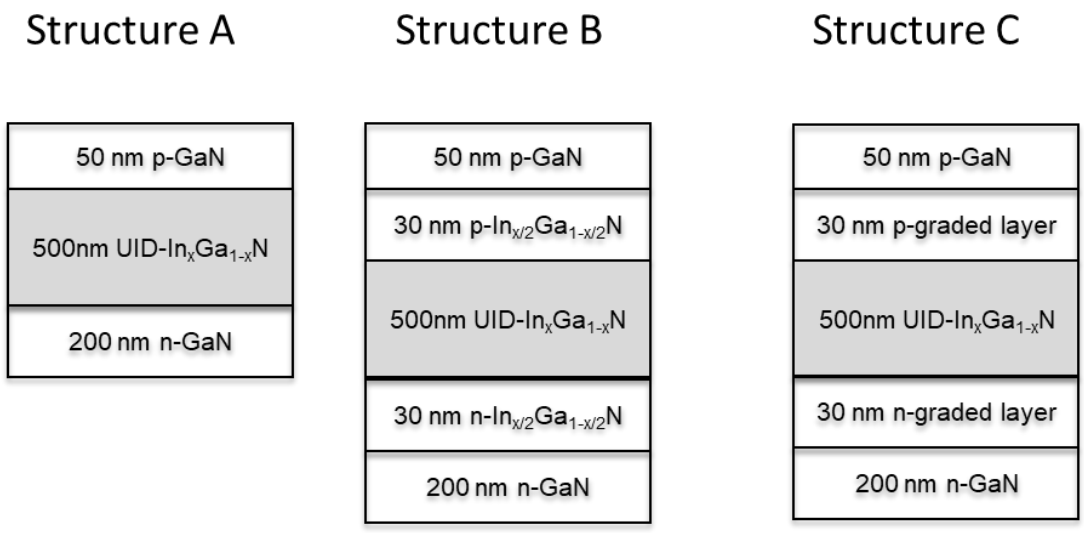

Figure 2.6. Schematic diagrams of $GaN/In_xGa_{1-x}N/GaN$ base structure (Struture A), base structure with $In_{x/2}Ga_{1-x/2}N$ interlayer (Structure B) and base with graded layers (Structure C: Indium grade from 0 to x in top interface and grade from x to 0 in bottom interface)

assumed as 174 meV. Impact ionization of holes in p-GaN exponentially increases with temperature, leading to 1% ionization at room temperature and ~20% ionization at 450 °C [40].

Figures 2.5(a) and (b) show the efficiency and short-circuit current as a function of Indium composition for the p-GaN/UID-$In_xGa_{1-x}N$/n-GaN structure. The efficiency first increases with Indium composition due to the decrease of the InGaN bandgap in the base. The efficiency peaks at an Indium composition ~$In_{0.2}Ga_{0.8}N$, after which it falls steeply as the potential barriers' height becomes too large due to band offset and polarization effects (Figure 2.7). These potential barriers are believed to prevent carrier transport in the device. Figure 2.5(c) shows that polarization-induced field opposes the photo-carrier collection, resulting in an abrupt drop in the current density for large Indium compositions. To mitigate the polarization and band offset effects, band engineering techniques were adopted. Figure

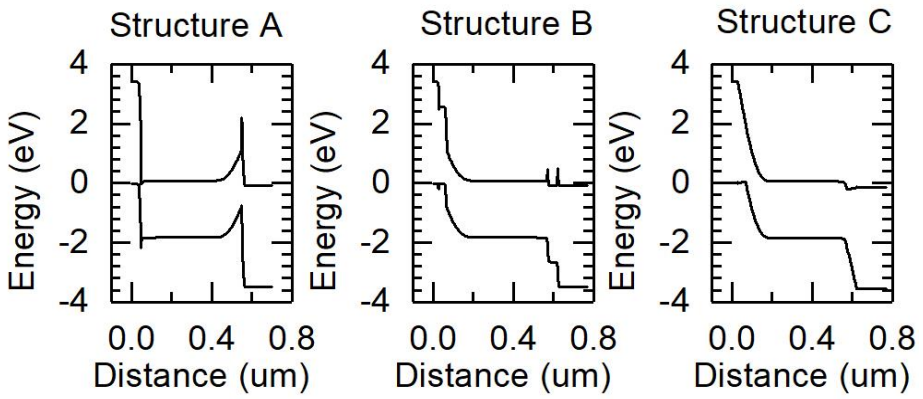

Figure 2.7 Energy band diagrams of various GaN/InGaN/GaN solar cell structures from Figure 2.6

2.6 shows three different 1J InGaN hetero-structures which have been investigated in simulation. From Structure A to Structure B, interlayers with half Indium composition compared to the base absorber are added into the hetero-interfaces. In Structure C, Indium compositional grading layers are added into the hetero-interfaces in order to fully relax the potential barriers in the hetero-interfaces. The band diagram in Figure 2.7 shows that in Structure B, barriers are somehow relaxed by spreading them out among one or more hetero-interfaces. In Structure C, the band offset and polarization effects are totally mitigated with compositional graded layers. As shown in Figure 2.8, the efficiency of Structure B with an interlayer is improved compared to Structure A, and did not fall steeply until ~$In_{0.35}Ga_{0.65}N$ at 300 K. From room temperature to 450 °C, the efficiency of the devices seriously degrades, especially due to the decrease of V_{oc} (open circuit voltage) under high temperature, as shown in the following equation:

$$V_{oc} = \frac{nkT}{q} \ln\left(\frac{J_{sc}}{J_0} + 1\right) \tag{2.24}$$

where, n and k are the diode quality factor and the Boltzmann' constant, respectively.

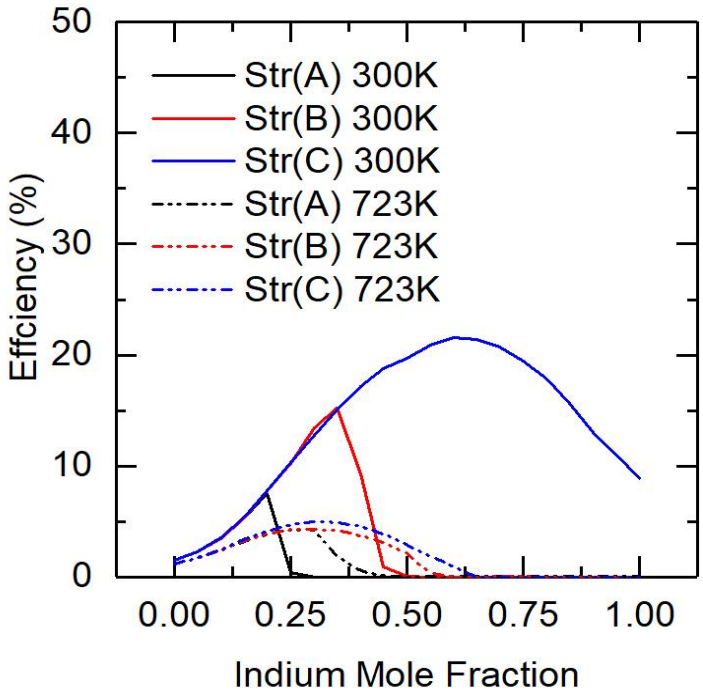

Figure 2.8. Efficiency as a function of Indium Mole Fraction of various GaN/InGaN/GaN solar cell structures from Fig. 3 under room temperature(300K) and 450 °C(723K), 1X AM1.5.

The reverse saturation current density, J_0, increases with intrinsic carrier concentration n_i at high temperatures:

$$J_0 \propto n_i^2 \tag{2.25}$$

where n_i^2 is given by

$$n_i^2 = N_C N_v \cdot e^{-\frac{E_g}{kT}} = 4\left(\frac{2\pi k}{h^2}\right)^3 m_n^{\frac{3}{2}} m_p^{\frac{3}{2}} T^3 e^{-\frac{E_g}{kT}} \tag{2.26}$$

Larger J_0 causes a degradation of V_{oc} and the cell conversion efficiency at high temperatures. Even for Structure C with an Indium mole fraction higher than 0.60, the efficiency of the devices is reduced to ~0. Note that, for Structure A (Base device) and Structure B (base device with an interlayer), the performance is improved at large Indium

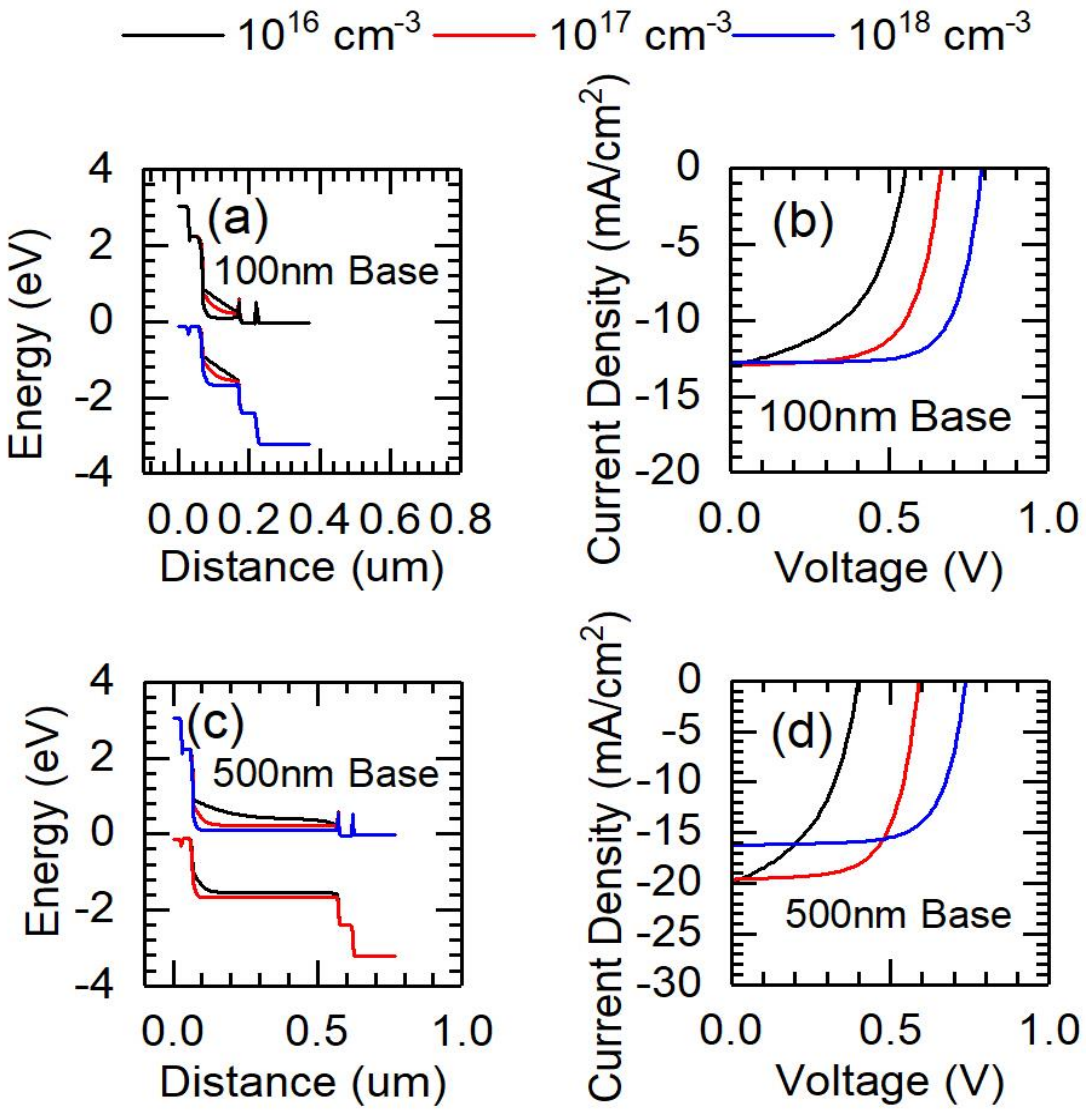

Figure 2.9 Energy band diagrams and the corresponding IV curves for $In_{0.4}Ga_{0.6}N$ devices with base thickness (100 nm and 500 nm) and doping concentration (10^{16} cm^{-3}, 10^{17} cm^{-3} and 10^{18} cm^{-3}) under 450 °C, 1sun.

Mole fractions compared with room temperature. From room temperature to 450 °C, the cut-off Indium mole fraction is improved from ~0.25 to ~0.4 for Structure A and from ~0.45 to ~0.60 for Structure B, respectively. It is due to the fact that thermionic emission

and tunneling effects at hetero-interfaces under high temperatures are more pronounced compared with 300 K and more photocurrent can be transported across the hetero-interfaces. It leads to an efficiency of Structure B slightly lower but very close to Structure C under 450 °C. Since a high quality compositional grading layer is much more difficult to achieve in practice, designs based on Structure B with one $In_{x/2}Ga_{1-x/2}N$ interlayer at hetero-interface is adopted and will be optimized for the 1J solar cell at 450 °C.

Figure 2.9 shows the energy band diagrams and the corresponding IV curves for $In_{0.4}Ga_{0.6}N$ devices based on Structure B with different UID-thicknesses and donor concentrations at 450 °C. The device efficiency is affected by the thickness and doping of the UID-layer. As the thickness of the base InGaN layer increases, more photons can be absorbed, resulting in increased J_{sc}. However, when base doping increases, the collection efficiency drops due to the narrower depletion width, resulting in decreased J_{sc}. In contrast to J_{sc}, V_{oc} slightly decreases with base thickness, but it rises as the base doping increases with the narrower depletion region width. The saturation current density J_0 can be calculated as [8]

$$J_0 = qn_i w/\sqrt{\tau_e \tau_h} \tag{2.27}$$

where n_i is the intrinsic carrier concentration, τ_e and τ_h are the electrons and holes lifetimes, respectively, and w is the width of the depletion region. As shown in Figure 2.9, for 100 nm base devices, the base doping has negligible impact on J_{sc} since the width of un-depleted region is relatively small compared with the diffusion length even under high base doping. V_{oc} is improved with high doping as expected. However, for 500 nm base devices, J_{sc} degrades at 10^{18} cm^{-3} since most of the base region is un-depleted and suffers from a low collection efficiency. Thus, a trade-off between base thickness and doping should be

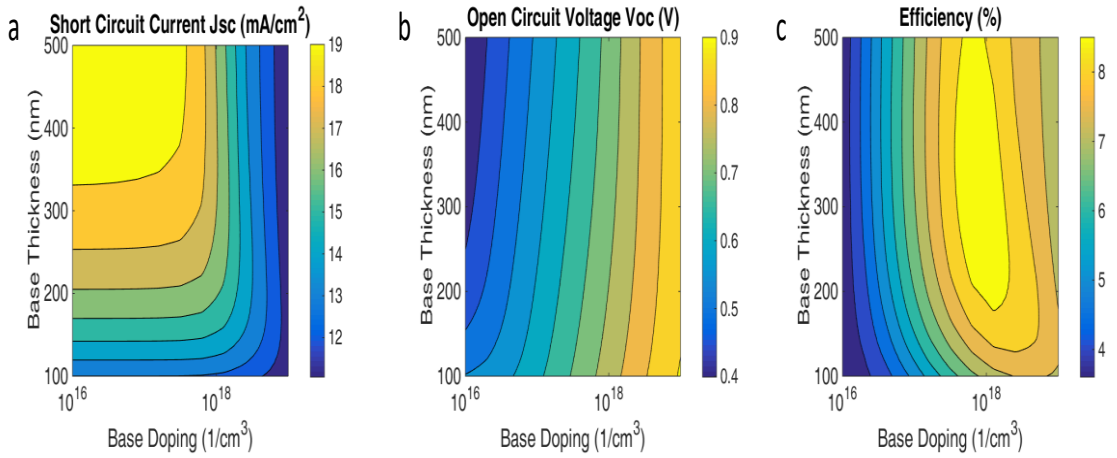

Figure 2.10 Contour plot Jsc(a), Voc(b) and efficiency(c) with various base thickness and doping for $In_{0.4}Ga_{0.6}N$ devices under 450 °C.

taken in order to optimize the performance of these solar cells. Figure 2.10 depicts the 2D contour plot of J_{sc}, V_{oc} and Efficiency for different base thicknesses and doping concentrations for precise optimization. The optimized device demonstrates 8.8% efficiency under 1 sun with a base doping and thickness of 7×10^{17} cm^{-3} and 340 nm, respectively. However, this performance is still inadequate for a high efficiency 1J solar cell application at high temperatures.

To determine the limit of the high temperature solar cell performance, the impact of light concentration and SRH lifetime were also investigated. As showed in Figure 2.11, J_{sc} from a solar cell depends linearly on incoming light intensity (concentration). However the incident power also increases linearly with concentration, thus J_{sc} effect does not provide an efficiency increase. Instead, V_{oc} increases logarithmically with concentration, as shown below:

$$V_{oc'} = V_{oc} + \frac{nkT}{q} lnX \tag{2.28}$$

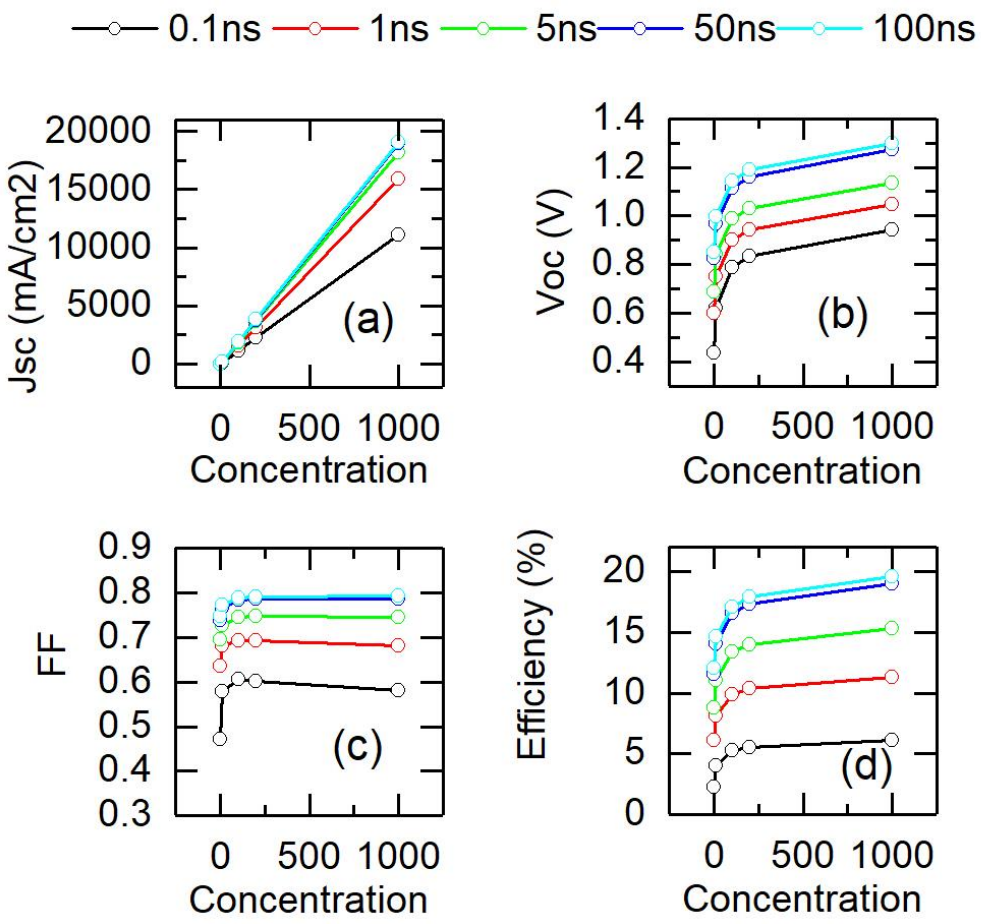

Figure 2.11 J_{sc}, V_{oc}, *FF* and Efficiency of optimized $In_{0.4}Ga_{0.6}N$ cell under various light concentration and SRH lifetime.

where *X* is the concentration of the light. On the other hand, the efficiency will also increase with SRH lifetime. Long SRH lifetime requires a high quality InGaN absorber. From Equation (2.27), J_0 will decrease with lifetime and will improve V_{oc}. Since at high temperatures, J_0 increases with intrinsic carrier concentration n_i, this results in a poor V_{oc} and efficiency. Thus the V_{oc} recovery from concentration and SRH lifetime is essential for

high efficiency solar cells at high temperatures. With a 100 ns SRH lifetime and at 1000 suns (concentration), the efficiency improved from 8.8% (5ns, 1sun) to 19.6%.

2.5 1J Multiple Quantum Well Top Cell

Besides bulk device configurations, one alternative design for wide bandgap top cells is to leverage the MQW or SL(super lattice) technology. The epitaxial growth of InGaN is challenging because of the large lattice mismatch between InN and GaN as mentioned before. These issues make growing thick and high crystal quality InGaN absorber layers with a relatively high Indium composition very difficult. Generally speaking, the critical thickness of InGaN decreases rapidly with increasing Indium composition. When the thickness of InGaN exceeds its critical value, the lattice relaxes through dislocation formation, which act as recombination centers, degrading the performance of the device. One way to mitigate this problem is to utilize multiple quantum well (MQW) structures. However, the carrier trapping inside the quantum wells due to quantum confinement can seriously limit the performance of MQW devices. In addition, spontaneous and strain induced polarization exists in the InGaN/GaN MQW devices, which increases with increasing Indium composition. Despite of these challenges, MQW device show the feasibility for top cells with larger bandgap InGaN (lower barrier height) design since quantum confinement effects are not as pronounced as in the bottom cell (larger Indium composition and barrier height).

The simulated cell layer structure is illustrated in Figure 2.12(a). Briefly, the active optical absorption region consists of 40 periods of $In_{0.12}Ga_{0.88}N$ (3 nm) /GaN (2 nm) MQWs. The barrier thickness was designed to be relatively small to enhance current tunneling among quantum wells and improve the collection probability of the photo-generated carriers. The

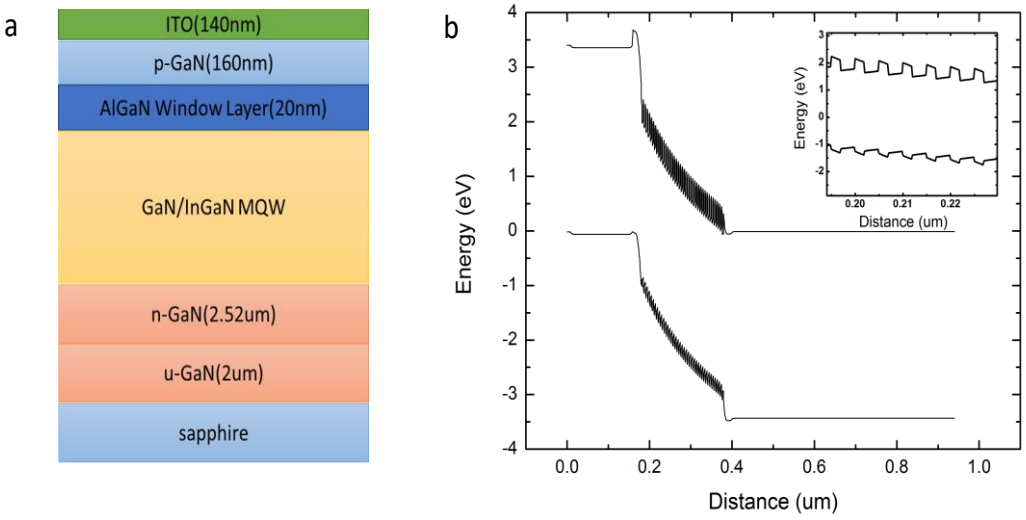

Figure 2.12 (a) Schematic diagram of the InGaN/GaN multi quantum well structure. (b) Simulated band diagram of the investigated device. Figure inset shows the detailed band diagram of each quantum well.

device structure was grown on a GaN/sapphire template with 2 μm-thick undoped GaN layer. The thickness of the p-GaN (n-GaN) is ~160 nm (~2.52 μm). On top of the MQW region, a 20nm p-doped AlGaN layer is grown as a window layer which can prevent minority carriers from entering front surface. Finally, 140 nm of ITO is deposited, which serves as a current spreading layer. Figure 2.12(a) shows the simulated band diagram of the investigated device structure under zero bias condition. The detailed band diagram shown in the inset of Figure 2.12(b) shows that the polarization induced electric field inside the quantum well opposes the built-in electric filed of the p-n junction. This leads to a decrease in the overall carrier collection efficiency among the quantum wells which results in a reduction of the photocurrent. The quantum barriers also trap the photo-generated carriers in the wells. Due to the high recombination rate, which originates from SRH, Auger

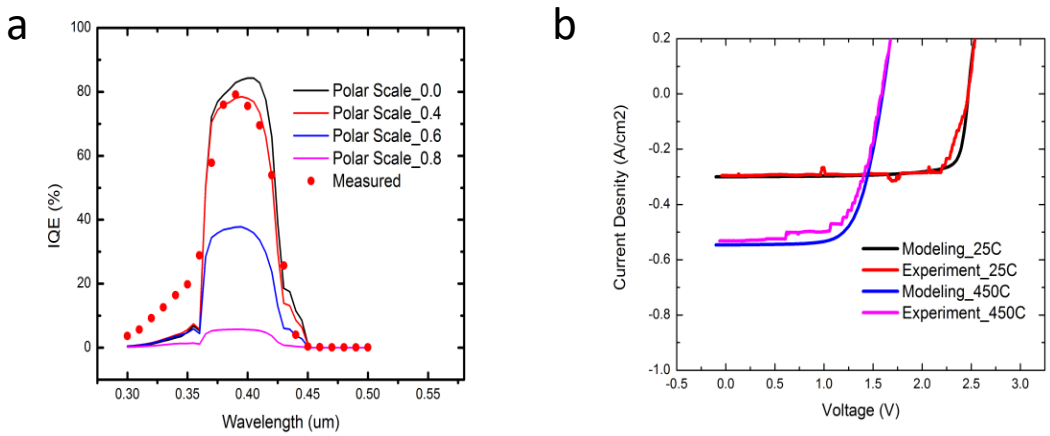

Figure 2.13 (a) IQE of the investigated device at room temperature. The main parameter is the polarization screening factor (polar scale). With polar scale 0.4, the modeling results match very well the experimental data. (b) Experimental and simulated IV curves at 25 °C and at 450 °C, 300 suns.

and band-to-band recombination mechanisms, large amounts of photo-carriers will recombine inside the quantum well, thus limiting the performance of the MQW solar cell devices. Figure 2.13(a) shows the IQE of the simulated device at room temperature for different polar scales. With polar scale 0.4, the simulation is in very good agreement with measured data. As seen, the simulated IQE decreases with increasing polar scale (increasing interface polarization charge). For a polar scale equal to 0.8, very few of the photo-generated carriers are collected. For a polar scale equal to 0, zero polarization charges will be placed in the hetero-interface and IQE is improved by ~5%. Figure 2.13(b) shows the I-V curves of the investigated devices at 25 °C and at 450 °C under 300X AM1.5 illumination. Modeling and experiment show good agreement. From room temperature to 450 °C, the short circuit current (J_{sc}) increases from 0.3 A/cm^2 to 0.53 A/cm^2 due to the red shift of bandgap edge at high temperatures. V_{oc} decreases from 2.47 V to 1.59 V and the

Fill Factor (FF) decreases from 0.86 to 0.66. The efficiency drops from 2% to 1.87% from 25 °C to 450 °C.

CHAPTER 3

TANDEM 2J SOLAR CELL SIMULATION

3.1 Polarization Engineered Tunnel Junction

Tunnel junctions are crucial in the design of multi-junction solar cells. It provides a low electrical resistance between two sub-cells. There are challenges with III-nitrides (specifically Ga(Al)N) based tunnel junctions. One of them is the wide bandgap of nitrides which results in a low tunneling probability and hence a high tunneling resistance. Consequently, the photo-voltage would be lower since some voltage drops across the tunnel junction. Recently, polarization engineering was proposed for nitride tunnel junctions [41]–[43]. GaN/InGaN/GaN junctions that have interfacial polarization-induced dipoles reduce the depletion width. Furthermore, a thin layer of InGaN with a lower bandgap will also lead to a lower tunneling barrier. With these benefits, GaN/InGaN/GaN structures can serve as a high current density tunnel junctions or tunnel diodes with negative differential resistance in their forward IV characteristics.

In this work, the author used a n-GaN/i-$In_{0.5}Ga_{0.5}N$/p-GaN tunnel junction for reduced tunnel resistance. Figure 3.1 shows the equilibrium band diagram of the investigated tunnel junction. Band bending at the hetero-interface is caused by the polarization change and band offsets. The I-V characteristics of the tunnel junction are shown in Figure 3.2. By increasing the n and p doping of the GaN regions to 5×10^{19} cm^{-3}, a very low resistance junction was realized. Heavy doping causes the depletion width as well as the tunnel distance to be reduced. Then tunnel probability will be improved. Negative differential resistance behavior shows up in forward bias characteristics. Thus, the tunnel current density is increased with the doping density. From the I-V curve, the voltage loss across

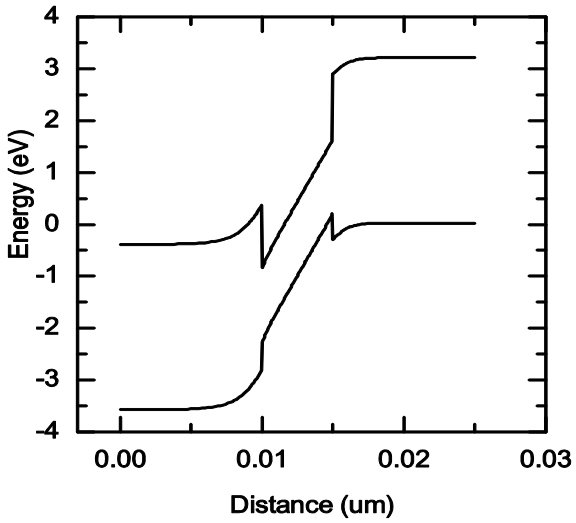

Figure 3.1 Energy band diagram of a polarization engineered p-GaN/i-InGaN/n-GaN tunnel junction device.

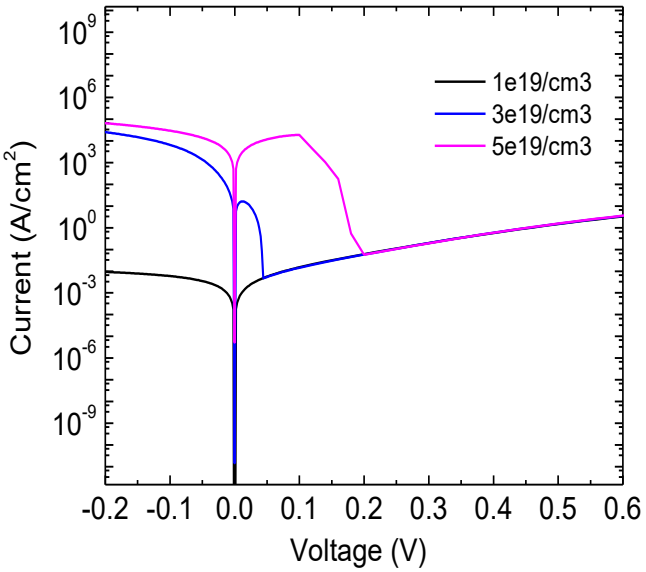

Figure 3.2 IV curves for n-GaN/i-InGaN/p-GaN tunnel junction with different GaN doping level.

tunnel junction at 1000 mA/cm^2 is ~1 mV at a doping level of 5×10^{19} cm^{-3}. Thus, a

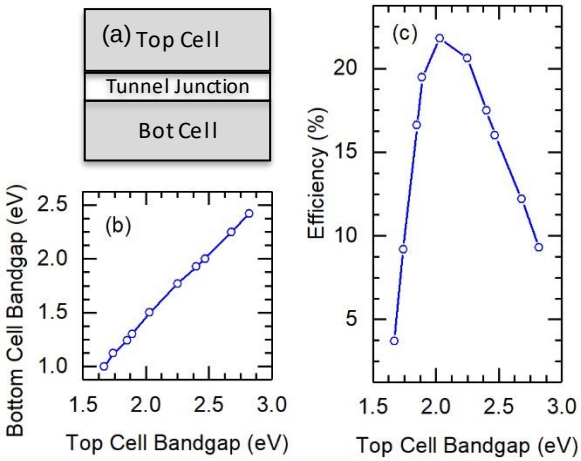

Figure 3.3 (a) Efficiency as a function of top cell bandgap. The optimized bandgaps are 2.03 eV and 1.50 eV for top cell and bottom cell, respectively. (b) IV curves for top cell (2.03 eV), bottom cell (1.50 eV) and the combined tandem cell.

promising tunnel junction is demonstrated for sub-cell connections in multi-junction solar cells based on simulation design.

3.2 Tandem Cell Current Matching Design

Based on the design consideration discussed previously, from the 1J modeling and the tunnel junction design, we simulated the basic tandem structure shown below in Figure 3.3(a) assuming 100ns SRH lifetime and under 200X illumination. Figure 3.3(b) shows the combination of bandgaps for the top and bottom cells used in the simulation in order to give the optimized efficiency. For a specific top cell bandgap, a fixed bandgap of the bottom cell was selected for current matching and best Voc. The integrated photon flux of the bottom cell bandgap from the spectrum should be approximately twice as much as top cell bandgap, theoretically without top cell filtering. Then the bottom cell will generate the same amount maximum light current from the filtered spectrum by the top cell and

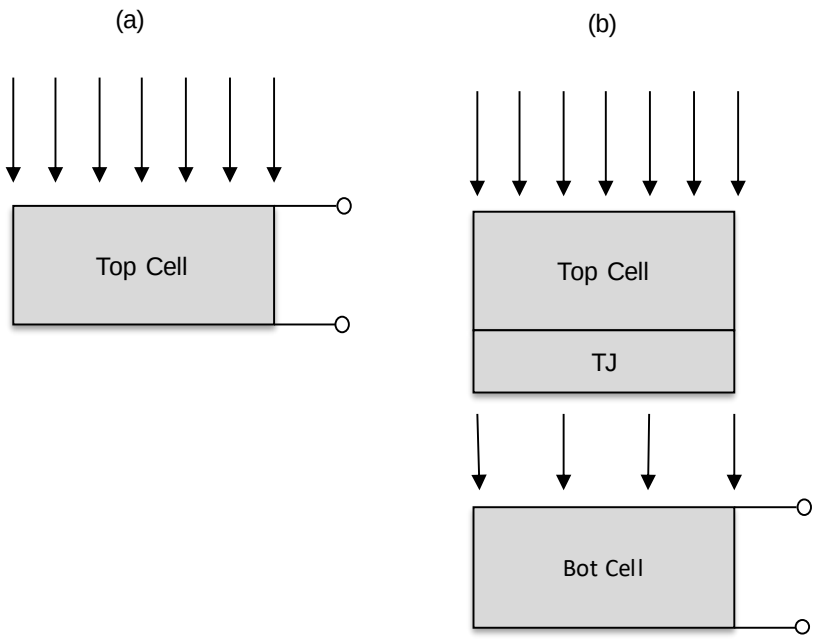

Figure 3.4 Schematic structures of (a) the top cell and (b) the bottom cell for current matching procedure.

maintain current matching for the tandem cell design. If the bottom cell's bandgap is too small, current matching even could be achieved via thinning the bottom cell thickness, however, there will be Voc loss due to an un-optimized (smaller) bottom cell bandgap. Figure 3.3(c) shows the efficiency as a function of top cell bandgaps. The efficiency peaks at 21.8% with a 2.03 eV top cell and a1.50 eV bottom cell, then drops steeply to 3% from the 2.03 eV top cell ($In_{0.30}Ga_{0.70}N$) to 1.74 eV top cell ($In_{0.43}Ga_{0.57}N$) due to the polarization and band offset effects at high indium composition, especially for low bandgap bottom cells. Thicknesses for both sub-cells have been optimized for the best efficiency. Each sub-cell is simulated separately as shown in Figure 3.4. Since the thickness variation of the top cell will influence the remaining light left for bottom cell, the top cell's solar response is investigated first under a 200 X AM1.5 full spectrum (Figure 3.4 (a)). Then the bottom

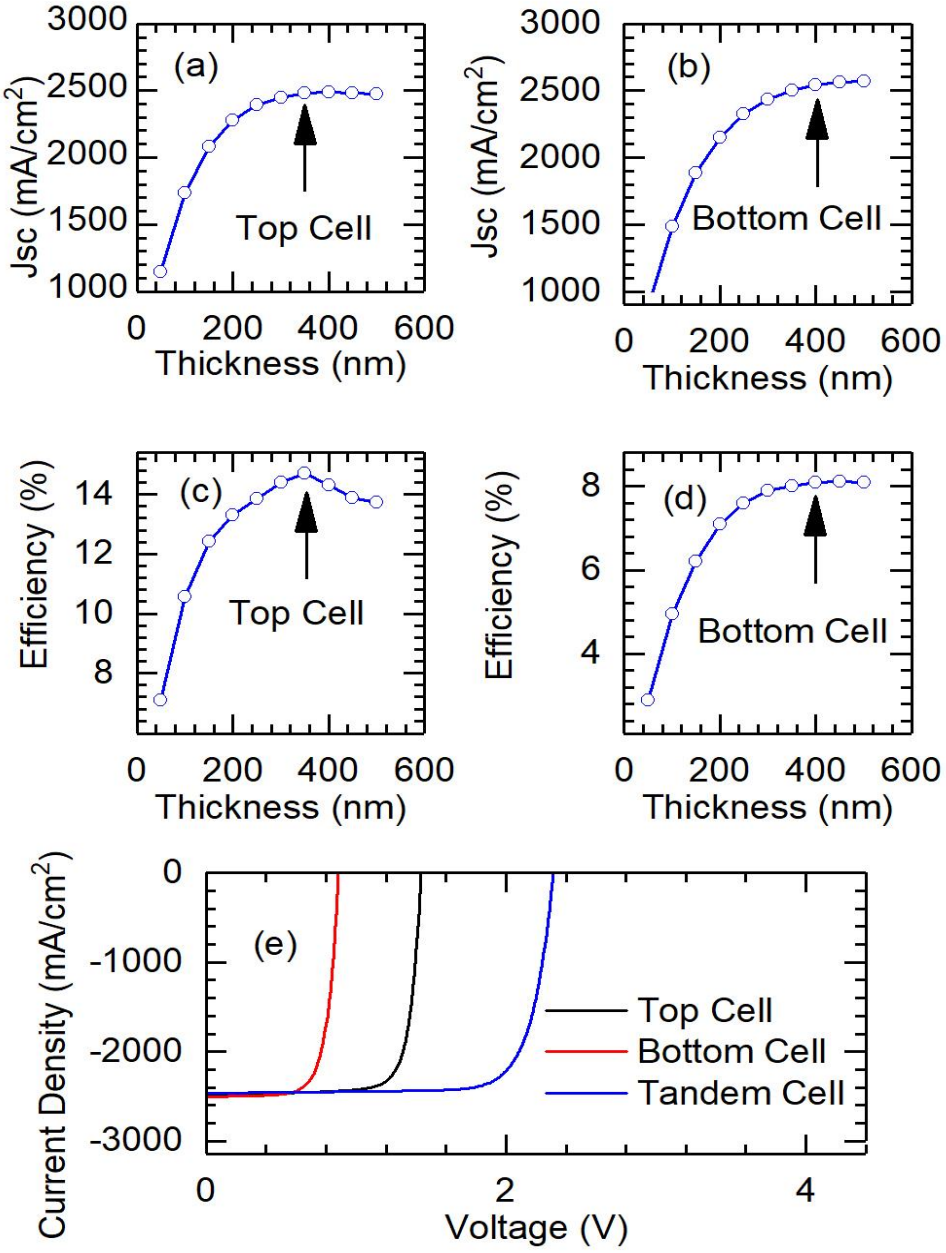

Figure 3.5 (a)-(d) Jsc and efficiency as a function of base thickness for both the top (2.03 eV) and bottom cell (1.50 eV). (e) J-V curves of the current matched tandem cell under 200-suns, 450 C with SRH lifetime 100ns.

cell's performance is evaluated under the filtered spectrum from the top cell and tunnel

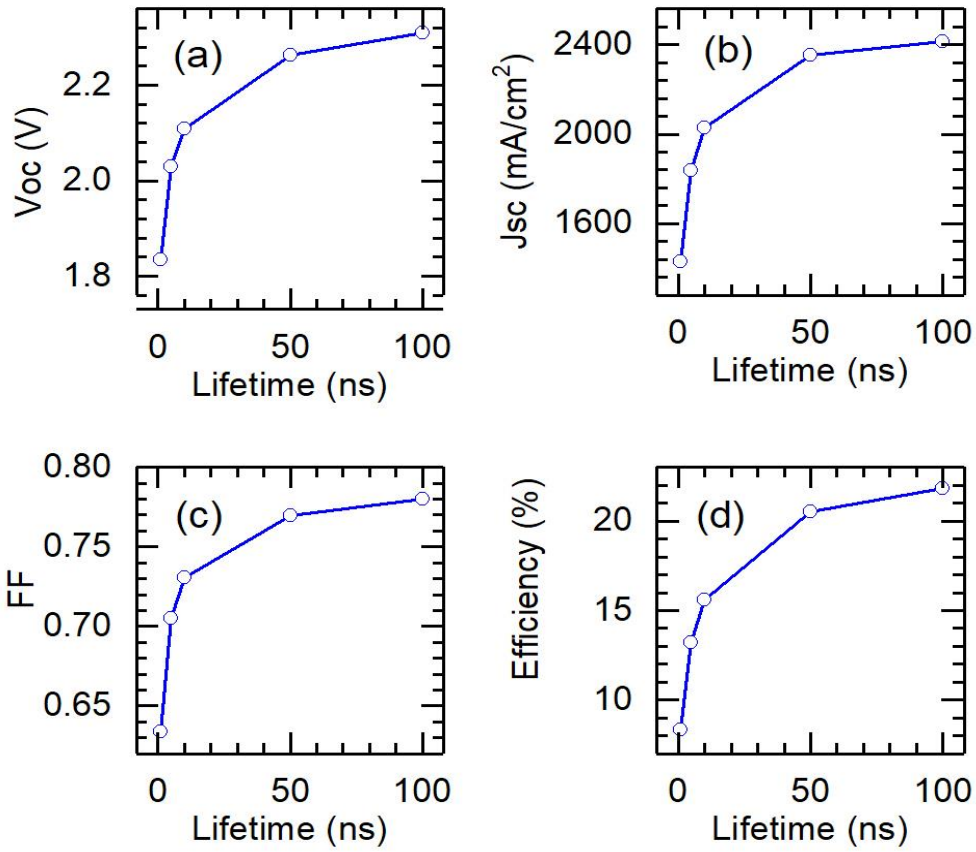

Figure 3.6 (a) Voc, (b) Jsc, (c) Fill Factor and (d) efficiency of the current matched champion cell as a function of SRH lifetime.

junction (Figure 3.4(b)). As shown in Figure 3.5 (a) and (c), an optimal Jsc (~2490 mA/cm^2) is obtained for top cell with a base thickness of 350 nm, resulting in 14.7% efficiency. The bottom cell base thickness will be tuned until the same Jsc is achieved for current matching. With a bottom cell base ~400 nm, the same amount of Jsc could be obtained, resulting in 8.0% from the filtered spectrum for a 1J bottom cell. The J-V characteristics of the thickness-optimized 2J cell and its sub-cells under 200-suns illumination and 450 °C are shown in Figure 3.5(e). Photocurrent matching between the two sub-cells is clearly observed through the J-V curves. The V_{oc} of the top and bottom

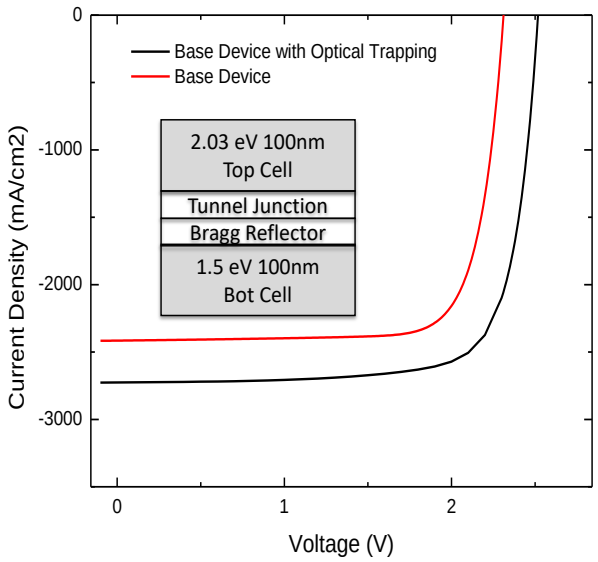

Figure 3.7 Compare of IV curves of optimized devices with and without optical trapping and thinner (reduced from 350nm to 100nm) base absorber device

cell are 1.44 V and 0.88 V, respectively. The optimal V_{oc} of the tandem cell is then ~2.32 V. Therefore, the stacking up of V_{oc} from subcells leads to higher efficiency for the target tandem cell. Figure 3.6 shows V_{oc}, J_{sc}, Fill Factor and the efficiency as a function of the SRH lifetime for the champion tandem cell. All the investigated solar parameters are increasing with longer SRH lifetime due to reduction of recombination loss. From 1ns to 100 ns, the conversion efficiency improves from 8.32 % to 21.8%. Note that, with the SRH lifetime (5 ns) for InGaN growth achieved to date, 13.2% efficiency is obtained.

Light trapping can be implemented with a thinner film base absorber but still maintain Jsc. V_{oc} could benefit from a thinner base absorber according to Figure 2.10(b) and result in an improved efficiency. In this simulation, light is incident from the top on the wide-gap cell. Light trapping with an average of 10 reflections (less than the Lambertian limit ~$4n^2$)[44] is modeled in each cell, and an ideal Bragg reflector separates the top and bottom cells

TABLE IV
Solar cell characteristics of the investigated champion cell.

Devices	Subcell absorber thickness(nm)	J_{sc} (mA/cm2)	V_{oc} (V)	FF	Efficiency (%)
Base device	350	2455	2.31	0.779	21.8
Base w/ Optical Trapping	100	2725	2.52	0.766	26.3

optically, which reflects 100% of the light above the bandgap of the top cell and transmits 100% below the bandgap. As shown in Figure 3.7 and Table 4, with optical trapping and an absorber thickness reduced from 350 nm (400 nm) to 100 nm, the efficiency is improved from 21.8% to 26.3%. Even with a thinner absorber, since the effective optical path has been increased, J_{sc} does not decrease, but actually increases from 2455 to 2725 mA/cm^2. V_{oc} is improved from 2.31 V to 2.52 V due to a reduced saturation current, J_0, with narrower base.

3.3 Alternative Configurations for Multiple Junction Solar Cells

Besides monolithic multiple junction solar cells connected via a tunnel junction connection, another common configuration for multi-junction (MJ) solar cells is the mechanically connected MJ solar cells. Unlike monolithic multiple junction devices with just one terminal and strictly relying on current matching between sub-cells, mechanical MJ solar cell have multiple terminals. With the photo-current extracted separately, current matching is not crucial. In this work, a new path for constructing MJ InGaN solar cells is proposed. Due to the growth challenge for high quality thick InGaN film as mentioned before in this dissertation, tunnel junctions can be leveraged to split a 1J cell into several sub-cells with the same bandgap. With this design, multiple thinner InGaN films can be used in each subcell and make the best use of the spectrum beyond its bandgap. Thus, it

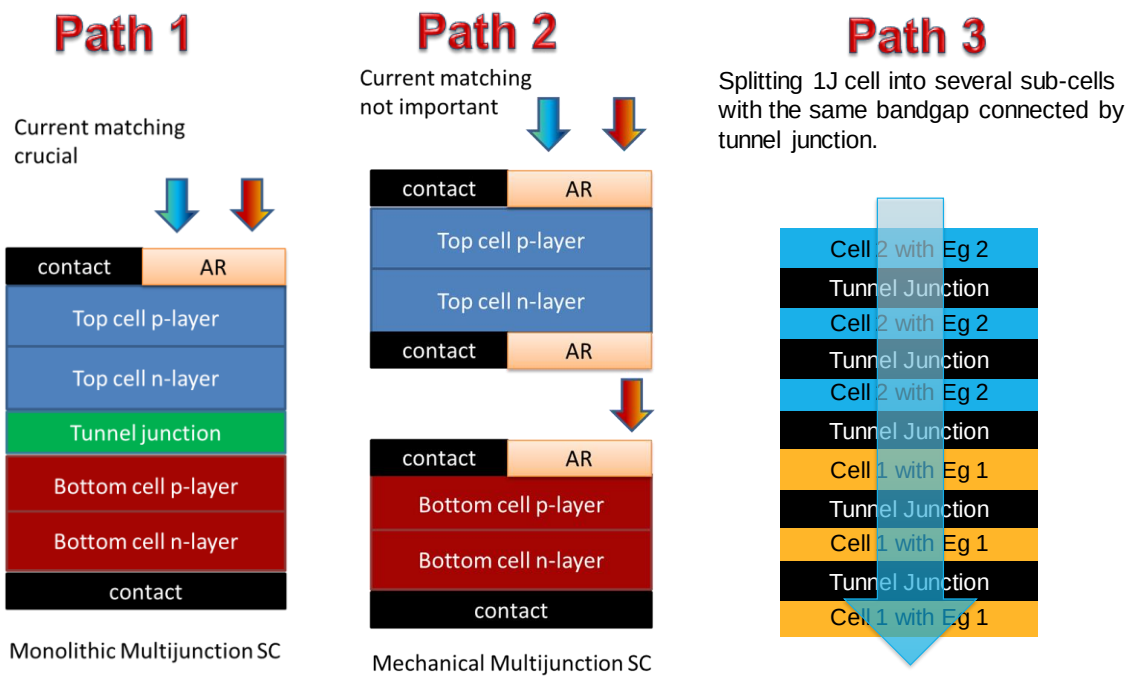

Figure 3.8 Three different paths for realizing multi-junction solar cells. Path 1 is a monolithic multi-junction design in which current matching is crucial and a tunneljunction is required. Path 2 represents a mechanical multi-junction design. In this configuration, each subcell has its own terminal making current matching unnecessary compared with Path 1. Finally, Path 3 leverages tunnel junction to split a 1J cell into several sub-cells with the same bandgap. It can bypass the challenges for thick InGaN growth.

can bypass the challenges for high crystal quality thick InGaN growth without losing absorbable incident light. All three MJ solar cell configurations are illustrated in Figure 3.8. As mentioned above, a 4-terminal mechanically bonded dual-junction cell was proposed as an alternative to the monolithic design. Compared with the monolithic design, multiple terminals have to be used, but the need for tunnel junctions and current matching is eliminated. Bragg-reflectors are introduced to ensure that the spectrum is divided into the corresponding sub cells. For an intermediate Bragg-reflector, the short wavelength light will be reflected back to the top cell (larger band gap) and long wavelength light will be transmitted through the Bragg-reflector and absorbed by bottom cell (smaller band gap).

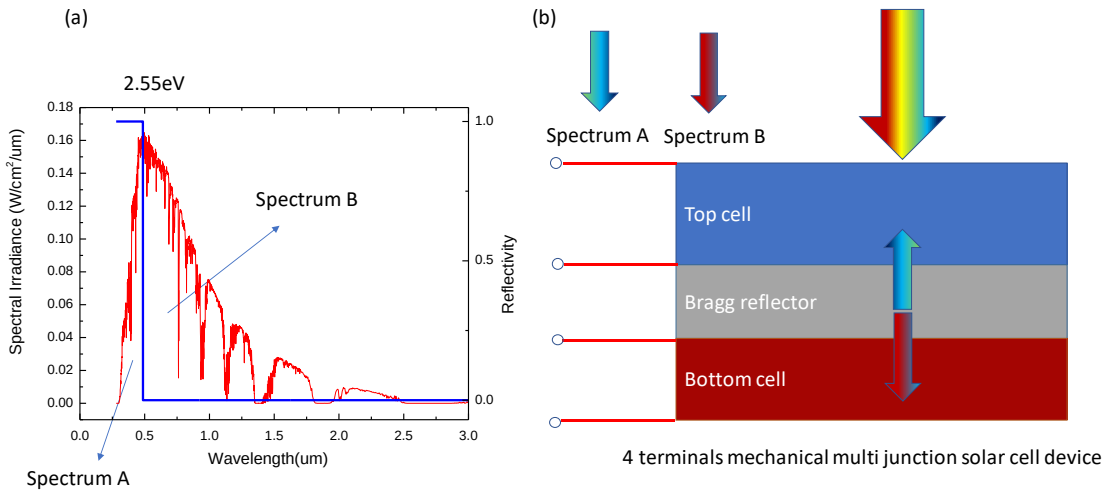

Figure 3.9 (a) Spectrum splitting approach for a mechanical MJ solar cell. Spectrum A corresponds to light with photon energy larger than top cell bandgap; Spectrum B corresponds to light with photon energy smaller than top cell bandgap (b) Schematic diagram of the 4 terminal mechanically coupled multi-junction solar cell device.

Figure 3.9(a) shows how spectrum is split by an ideal intermediate Bragg-reflector. The device is mechanically bonded and has 4 terminals for all sub-cells as shown in Figure 3.9(b). Then the bandgap of the top cell was chosen to be 2.55 eV at 450 °C, corresponding to the previously demonstrated bandgap by MOCVD technology[45]. We then varied the bandgap of the bottom cell to explore the variation in the total efficiency of the device. To be noted, the same light trapping method mentioned during the design of the monolithic MJ solar cell has also been implemented here. Figure 3.10(a) shows the I-V curves for the top cell assuming different trap limited lifetimes. When the lifetime increases, the current density of the top cell stays nearly the same. This is because with light trapping, the base thickness of the InGaN absorber is chosen to be 100 nm, which is less than the carrier diffusion length of ~500 nm. At the same time, Voc increases due to a smaller base thickness. In Figure 3.10(b), the efficiency first increases with In composition (decreasing

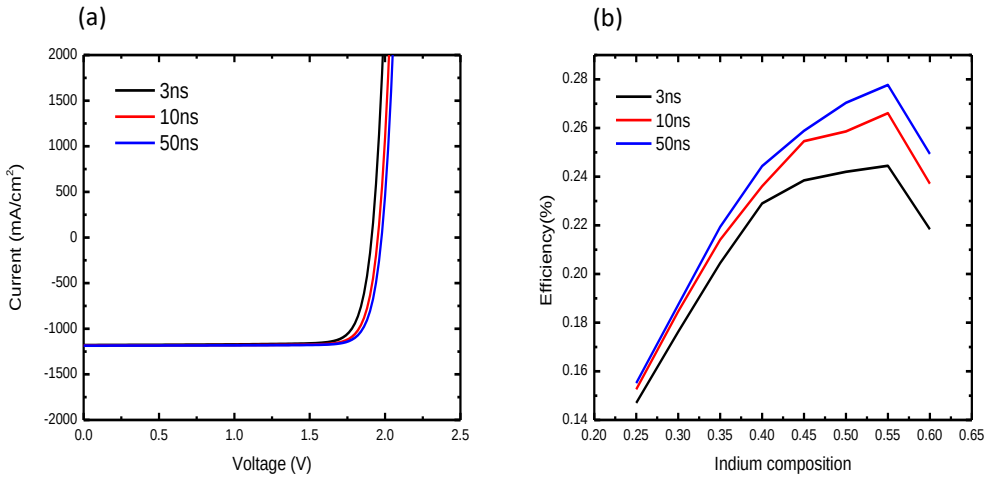

Figure 3.10 (a) IV curves FOR different lifetimes for a 2.55 eV top cell device at 450 °C, 200 X AM1.5. (b) Efficiency versus bottom Indium composition x. Solar cells with different material quality (SRH lifetime) are investigated at 450 °C, 200 X AM1.5.

band gap), reaches a maximum value for x=0.55, then starts to decrease due to polarization and band offset effects. The peak efficiency also improves with material lifetime. The simulated peak efficiency increases from 24% to 28% for SRH lifetimes ranging from 3ns to 50ns.

For path 3, shown in Figure 3.11(a), numerical simulation of a 4J solar cell with 3 bottom sub-cells at 450 °C, 200X, and 50ns SRH lifetime shows a 24% efficiency. The top cell bandgap is again chosen to be 2.55 eV. 3 bottom sub-cells with 1.7 eV are required to share the total incoming photon flux evenly for current matching. The thickness of each layer are optimized to ensure the Jsc generated from all sub-cells are the same each time one bottom junction is added to the device. From the black curve to the pink curve, Voc is improved when bottom cell junctions increase from 1 junction to 3 junctions. It is worth mentioning, for the bottom sub-cells, the thickess required for each sub-cell increases from top to

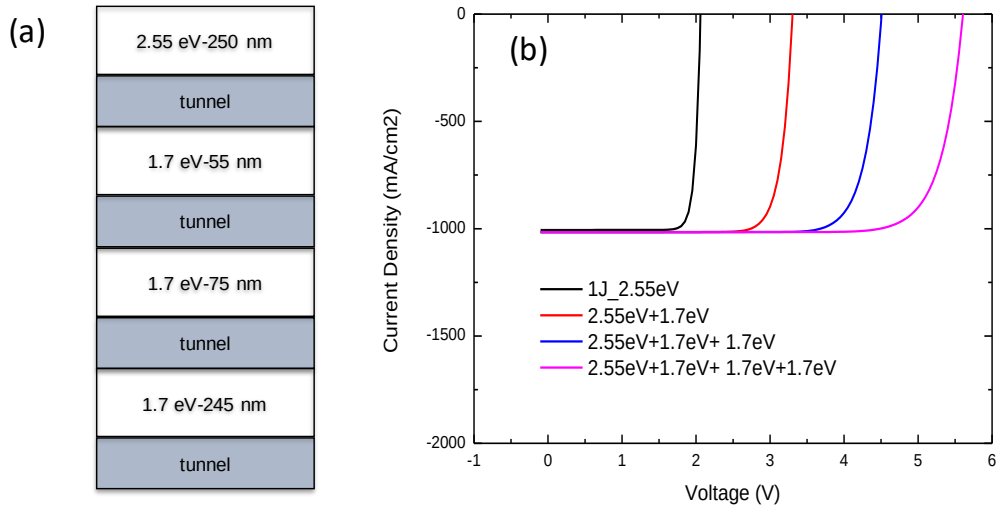

Figure 3.11 (a) Schematic diagram of the 4J solar cell connected by the tunnel junctions, with one 2.55 eV top cell, and three 1.7 eV bottom subcells. The thickness of each subcell are optimized for current matching. (b) Numerical simulation of 4J solar cell with 3 bottom subcells under 450 °C, 200X, and 50ns SRH lifetime shows 24%.

bottom. It is due to the fact , that during light incident from top to bottom, the absorption coefficient for short wavelength light is larger than light with energy closer to bandgap edge. Then the blue spectrum will be quickly absorbed. However, the longer wavelength spectrum is more resistant to absorption, and left for the next bottom cell requiring larger thickness for full optical absorption. Figure 3.11(b) shows that from the black curve to the pink curve, Voc is improved when the bottom cell junctions increase from 1 junction to 3 junctions. The whole 4J stack shows a Jsc of 1016 mA/cm^2, Voc of 5.61V, FF of 0.81 and energy conversion efficiency of 24%.

CHAPTER 4

OPTICAL MANAGEMENT

High efficiency solar cells require optimized optical management. An anti-reflection coating(ARC) should be designed properly to enhance optical absorption in the device. For the wide bandgap InGaN top cell, we proposed a double-layer ARC design which is optimized from 300nm to 500nm wavelength range. On the other hand, for the potential hybrid thermal system and tandem PV applications, the ARC design should be tailored for a broad wavelength range to utilize the whole spectrum. A triple-layer ARC [46] is adopted for low front reflection from 300nm to 1200nm wavelength range. In this chapter, the author will first introduce elementary optics theory, then illustrate the TMM (transfer matrix method) for multiple layer stack optical simulation, and finally cover the low reflection ARC design for InGaN/GaN solar cells.

4.1 Maxwell Equations

All classical electromagnetic phenomena including light reflection, absorption and transmission in PV cell design, are described by Maxwell's equations:

$$\nabla \times \mathrm{E} = -\frac{\partial B}{\partial t} \tag{4.1}$$

$$\nabla \times \mathrm{H} = \mathrm{J} + \frac{\partial D}{\partial t} \tag{4.2}$$

$$\nabla \cdot \mathrm{D} = \rho \tag{4.3}$$

$$\nabla \cdot \mathrm{B} = 0 \tag{4.4}$$

where E and H are the electric and magnetic field intensities, respectively. The quantities D and B are the electric displacement and the magnetic induction. The quantity ρ is the

volume charge density and J is the electric current density of external charges. For a linear and homogeneous medium,

$$\mathrm{D} = \varepsilon \mathrm{E} \tag{4.5}$$

$$\mathrm{H} = \frac{\mathrm{B}}{\mu} \tag{4.6}$$

where ε, μ are the permittivity and permeability of the optical propagation medium. In the source-free regions of space, Maxwell equations yield:

$$\nabla \times \mathrm{E} = -\frac{\partial B}{\partial t} \tag{4.7}$$

$$\nabla \times \mathrm{B} = \mu\varepsilon \frac{\partial E}{\partial t} \tag{4.8}$$

$$\nabla \cdot \mathrm{E} = 0 \tag{4.9}$$

$$\nabla \cdot \mathrm{B} = 0 \tag{4.10}$$

Using the source-free Maxwell equations, one can eliminate the extra equations to get a single vector quantity of interest:

$$\nabla^2 \mathrm{E} - \mu\varepsilon \frac{\partial^2 E}{\partial t^2} = 0 \tag{4.11}$$

$$\nabla^2 \mathrm{B} - \mu\varepsilon \frac{\partial^2 B}{\partial t^2} = 0 \tag{4.12}$$

A uniform plane wave represents light from a very distant source, for example the sun. When light from the sun propagates in a linear and source-free medium, the above equations for a single frequency wave can be resolved as:

$$\mathrm{E}(\mathrm{r}, \mathrm{t}) = \mathrm{E}_0 e^{i(k \cdot r - wt)} \tag{4.13}$$

$$\mathrm{B}(\mathrm{r}, \mathrm{t}) = \frac{1}{v} \mathrm{E}_0 e^{i(k \cdot r - wt)} \tag{4.14}$$

With basic plane wave theory, one can deduce the laws for reflection and refraction of electromagnetic waves.

4.2 Fresnel's Equations for Normal Incidence

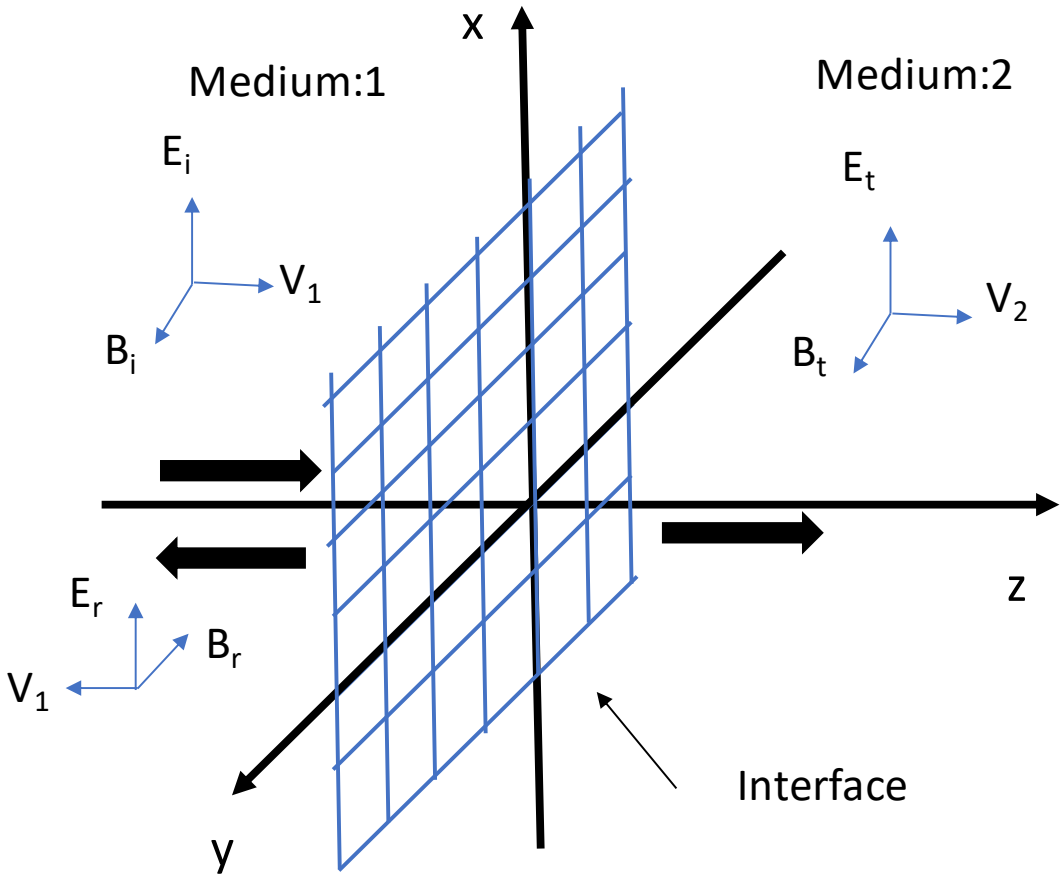

Figure 4.1 Normal incidence of a plane wave between two different material mediums.

Suppose a plane wave of frequency ω, traveling in the z direction and polarized in the x direction, propagates from medium 1 to medium 2 with normal incidence at the interface (Figure 4.1). The incoming light wave is given by:

$$\vec{\mathrm{E}}_i(\mathrm{z},\mathrm{t}) = \mathrm{E}_{0i}e^{i(k_1 z - wt)}\hat{x} \tag{4.15}$$

$$\vec{\mathrm{B}}_i(\mathrm{z},\mathrm{t}) = \frac{1}{v_1}\mathrm{E}_{0i}e^{i(k_1 z - wt)}\hat{y} \tag{4.16}$$

The reflected wave is given by:

$$\vec{\mathrm{E}}_r(\mathrm{z},\mathrm{t}) = \mathrm{E}_{0r} e^{i(-k_1 z - wt)} \hat{x} \tag{4.17}$$

$$\vec{\mathrm{B}}_r(\mathrm{z},\mathrm{t}) = -\frac{1}{v_1} \mathrm{E}_{0r} e^{i(-k_1 z - wt)} \hat{y} \tag{4.18}$$

It also gives rise to a transmitted wave into medium 2:

$$\vec{\mathrm{E}}_t(\mathrm{z},\mathrm{t}) = \mathrm{E}_{0t} e^{i(k_2 z - wt)} \hat{x} \tag{4.19}$$

$$\vec{\mathrm{B}}_t(\mathrm{z},\mathrm{t}) = \frac{1}{v_2} \mathrm{E}_{0t} e^{i(k_2 z - wt)} \hat{y} \tag{4.20}$$

where v_1 and v_2 are the speed of light in the corresponding medium, respectively.

Due to normal incidence, the electrodynamic boundary conditions for interface parallel vectors give that:

$$\mathrm{E}_{0i} + \mathrm{E}_{0r} = \mathrm{E}_{0t} \tag{4.21}$$

$$\frac{1}{v_1 \mu_1} (\mathrm{E}_{0i} - \mathrm{E}_{0r}) = \frac{1}{v_2 \mu_2} \mathrm{E}_{0t} \tag{4.22}$$

Based on the above equations, the outgoing amplitudes can be easily solved in terms of the incident amplitude:

$$\mathrm{E}_{0r} = \left(\frac{v_2 \mu_2 - v_1 \mu_1}{v_2 \mu_2 + v_1 \mu_1}\right) \mathrm{E}_{0i} \tag{4.23}$$

$$\mathrm{E}_{0t} = \left(\frac{2}{1 + \frac{v_1 \mu_1}{v_2 \mu_2}}\right) \mathrm{E}_{0i} \tag{4.24}$$

Since most media for solar cell system has a permeability μ are close to the vacuum value, with

$$\mu_1 \approx \mu_2 \tag{4.25}$$

$$\frac{v_1}{v_2} = \frac{n_2}{n_1} \tag{4.26}$$

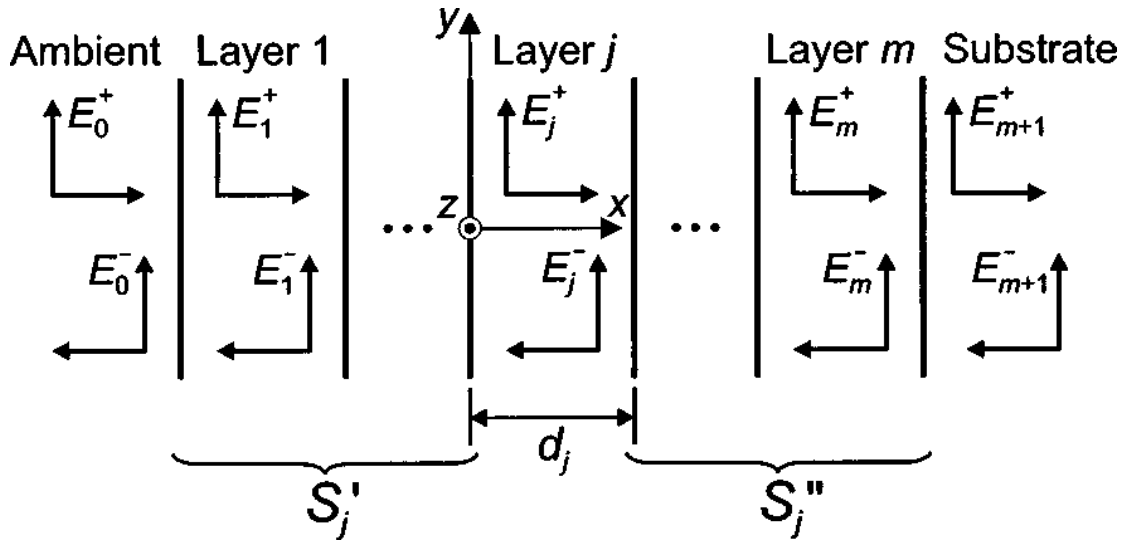

Figure 4.2 Schematic diagram of a multilayer structure with m layers between a semi-infinite transparent ambient and a semi-infinite substrate[47].

Equation 4.23 and 4.24 can be rewritten in terms of the refractive index,

$$\mathrm{E}_{0r} = \left(\frac{n_1 - n_2}{n_1 + n_2}\right) \mathrm{E}_{0i} \tag{4.27}$$

$$\mathrm{E}_{0t} = \left(\frac{2n_1}{n_1 + n_2}\right) \mathrm{E}_{0i} \tag{4.28}$$

The reflection coefficient, r, and transmission coefficient, t, of the incoming amplitude E_{0i} can then be expressed as:

$$r = \frac{n_1 - n_2}{n_1 + n_2} \tag{4.29}$$

$$t = \frac{2n_1}{n_1 + n_2} \tag{4.30}$$

These are known as Fresnel's equations for reflection and transmission.

4.3 Multilayer thin film reflection and transmission

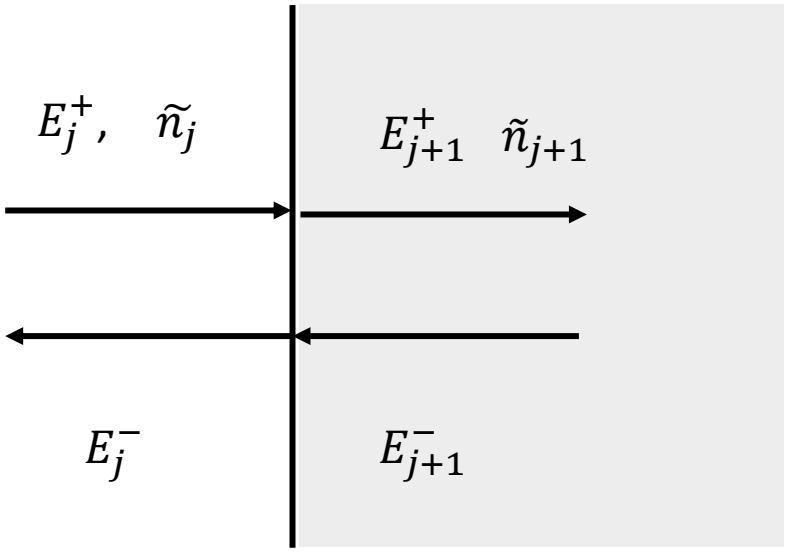

Figure 4.3 Schematic diagram for the electric field across the interface of the *j* layer and $j + 1$ layer.

Based on the theory of reflection and transmission at the interface of two different mediums, the transfer matrix method can be employed for multilayer calculations. Assuming isotropic and homogenous materials for the ARC design, propagation of light through the parallel-plane interfaces can be described by 2×2 matrices. As shown in Figure 4.2, an incoming plane wave is incident from the left ambient, and traverses a general multilayer structure with m layers and a semi-infinite substrate. For each layer j, the optical absorption has been considered in simulation via including the complex index of refraction $\tilde{n}_j = n_j + i\kappa_j$. n_j and κ_j is the refractive index and extinction coefficient as a function of wavelength for the material in the corresponding layer. As shown in Equations 4.17 and 4.18, magnetic field $\vec{B}$ is linearly propotional to the electric vector $\vec{E}$. For calculation simplification, only the optical electric field is illustrated in the TMM

calculation. The electric field vector consists of two components at a given position x for layer j : one component E_j^+ propagates in the positive x direction and the other E_j^- propagates in the negative x direction. Since the normally incident fields are tangential to the interface plane, the boundary conditions require that the electric field E and magnetic fields H be continuous across the sides of the interface as shown in Figure 4.3. In terms of the forward and backward electric fields, the continuity equations can be written as:

$$E_j^+ + E_j^- = E_{j+1}^+ + E_{j+1}^- \tag{4.31}$$

$$\frac{1}{v_1\mu_1}(E_j^+ - E_j^-) = \frac{1}{v_2\mu_2}(E_{j+1}^+ - E_{j+1}^-) \tag{4.32}$$

The above equations can be rewritten in a matrix form, with the fields E_j^+ and E_j^- on the left and E_{j+1}^+ and E_{j+1}^- on the right:

$$\begin{bmatrix} E_j^+ \\ E_j^- \end{bmatrix} = \frac{1}{t_{j,j+1}} \begin{bmatrix} 1 & r_{j,j+1} \\ r_{j,j+1} & 1 \end{bmatrix} \begin{bmatrix} E_{j+1}^+ \\ E_{j+1}^- \end{bmatrix} \tag{4.33}$$

where $r_{j,j+1}$ and $t_{j,j+1}$ are the Fresnel complex reflection and transmission coefficients defined by:

$$r_{j,j+1} = \frac{\tilde{n_j} - \tilde{n}_{j+1}}{\tilde{n_j} + \tilde{n}_{j+1}} \tag{4.34}$$

$$t_{j,j+1} = \frac{2\tilde{n_j}}{\tilde{n_j} + \tilde{n}_{j+1}} \tag{4.35}$$

Then Equation 4.33 then can be rewritten as

$$\begin{bmatrix} E_j^+ \\ E_j^- \end{bmatrix} = I_{j,j+1} \begin{bmatrix} E_{j+1}^+ \\ E_{j+1}^- \end{bmatrix} \tag{4.36}$$

where $I_{j,j+1}$ is interface matrix given by:

$$I_{j,j+1} = \frac{1}{t_{j,j+1}} \begin{bmatrix} 1 & r_{j,j+1} \\ r_{j,j+1} & 1 \end{bmatrix} \tag{4.37}$$

The propagation of light through layer j is described by:

$$L_j = \begin{bmatrix} e^{-ik_j d_j} & 0 \\ 0 & e^{ik_j d_j} \end{bmatrix} \tag{4.38}$$

where k_j is the wave vector given by:

$$k_j = \frac{2\pi}{\lambda}\tilde{n}_j \tag{4.39}$$

Since $\tilde{n}_j$ is the complex refractive index, $k_j d_j$ includes both the phase change and absorption decay during wave propagation in layer j. Then a total system transfer matrix S based on the interface matrix and the layer propagation matrix can relate the incident electric field from the ambient to the final transmitted electric field into substrate as:

$$\begin{bmatrix} E_0^+ \\ E_0^- \end{bmatrix} = S \begin{bmatrix} E_{m+1}^+ \\ E_{m+1}^- \end{bmatrix} \tag{4.40}$$

where S [47]is given by:

$$S = \begin{bmatrix} S_{11} & S_{12} \\ S_{21} & S_{22} \end{bmatrix} = \left(\prod_{j=1}^{m} I_{j-1,j} L_j\right) \cdot I_{m,m+1} \tag{4.41}$$

Assuming in semi-infinite substrate, no wave reflects backward, which means $E_{m+1}^- = 0$. Then the total reflection and transmission coefficient of the stratified multilayer structure can be simply calculated by the matrix elements of the total transfer matrix:

$$r = \frac{E_0^-}{E_0^+} = \frac{S_{21}}{S_{11}} \tag{4.42}$$

$$t = \frac{E_{m+1}^+}{E_0^+} = \frac{1}{S_{11}} \tag{4.43}$$

For now, we only know the total reflection and transmission of a complicate multiplayer structure. However, in solar cell device simulation, the internal electric field at a given

position should be also known for optical generation calculation. For the internal electric field derivation, one should divide the whole system into two subsets as shown in Figure 4.2. The first partial system starts from the ambient and ends at the layer *j-1* and layer *j* interface, with transfer matrix S_j'; the second partial system starts from the layer *j* and layer *j+1* interface, and ends at the substrate with transfer matrix S_j''. As shown in Figure 4.2, the two sub-systems are separated by layer *j*.

The first subset transfer matrix S_j' can be given as:

$$\begin{bmatrix} E_0^+ \\ E_0^- \end{bmatrix} = S_j' \begin{bmatrix} E_j'^+ \\ E_j'^- \end{bmatrix} \tag{4.44}$$

$$S_j' = \begin{bmatrix} S_{j11}' & S_{j12}' \\ S_{j21}' & S_{j22}' \end{bmatrix} = \left(\prod_{n=1}^{j-1} I_{n-1,n} L_n\right) \cdot I_{j-1,j} \tag{4.45}$$

where $E_j'^+$ and $E_j'^-$ is the forward and backward electric field at (*j-1, j*) interface for layer *j* left boundary.

Similarly, the second subset transfer matrix S_j'' can be given as:

$$\begin{bmatrix} E_j''^+ \\ E_j''^- \end{bmatrix} = S_j'' \begin{bmatrix} E_{m+1}^+ \\ 0 \end{bmatrix} \tag{4.46}$$

$$S_j'' = \begin{bmatrix} S_{j11}'' & S_{j12}'' \\ S_{j21}'' & S_{j22}'' \end{bmatrix} = \left(\prod_{n=j+1}^{m} I_{n-1,n} L_n\right) \cdot I_{m,m+1} \tag{4.47}$$

where $E_j''^+$ and $E_j''^-$ is the forward and backward electric field at the (*j, j+1*) interface for the layer *j* right boundary. For layer j, electric field ($E_j'^+$, $E_j'^-$) in the left boundary and the electric field ($E_j''^+$, $E_j''^-$) can be related with the nature of wave propagation in layer j:

$$E_j''^+ = E_j'^+ e^{ik_j d_j} \tag{4.48}$$

$$E_j''^- = E_j'^- e^{-ik_j d_j} \tag{4.49}$$

Combining Equations 4.44 to 4.49, the internal transfer coefficient which relates the incident light wave E_0^+ from the ambient to the local forward propagating electric field at the (*j-1, j*) interface can be derived as:

$$t_j^+ = \frac{E_j'^+}{E_0^+} = \frac{S_{j11}''}{S_{j11}''S_{j11}' + S_{j21}'S_{j21}''e^{2ik_j d_j}} \tag{4.50}$$

Similarly, the internal transfer coefficient which relates E_0^+ to the local backward propagating electric field at (j-1, j) interface can be derived as:

$$t_j^- = \frac{E_j'^-}{E_0^+} = t_j^+ \frac{S_{j21}''}{S_{j11}''} e^{2ik_j d_j} \tag{4.51}$$

With Equations 4.50 and 4.51, the electric field in any position of layer j can be expressed as:

$$\begin{aligned} E_j(x) &= E_j'^+(x) + E_j'^-(x) \\ &= (t_j^+ e^{ik_j x} + t_j^- e^{-ik_j x}) E_0^+ \end{aligned} \tag{4.52}$$

Thus, the expression for the total electric field in any position for a given layer j is derived. Given the magnitude of the optical field, the optical generation rate $\mathrm{G}_{opt}(j,x)$ for layer j at normal incidence is given by:

$$\mathrm{G}_{opt}(j,x) = \frac{1}{2} c \varepsilon_0 \alpha_j n_j \left|E_j(x)\right|^2 \tag{4.53}$$

where c is the speed of light, ε_0 is permittivity of free space, and α_j is the absorption coefficient for the given material of layer *j*, which can be calculated from the extinction coefficient κ as

$$\alpha_j = \frac{4\pi\kappa_j}{\lambda} \tag{4.54}$$

From Equation 4.53, it follows that the photo-generation rate is proportional to the magnitude squared of the electric field $\left|E_j(x)\right|^2$ and the absorption coefficient α_j.

4.4 Anti-reflection Design for Nitride Solar Cells

Based on the transfer matrix method illustrated above, the interference of light during propagation in materials is included for thin film ARC design. Figure 4.4(a) shows the optical constants of the materials used in the simulation. The optical constants of SiO_2, SiO_2-TiO_2 and Ta_2O_5 are obtained from Reference [48]. For GaN and $In_{0.12}Ga_{0.88}N$, the optical constants are measured by ellipsometric techniques. SiO_2-TiO_2 can be formed by the sol-gel method, and has the refractive index between the Ta_2O_5's and SiO_2's as shown in [48].

The thickness of each layer in the AR coating is optimized to minimize the front reflection loss current $\Delta J_{reflection\ loss}$ in the wavelength range from 300 to 1200 nm. The front reflection loss current is calculated from:

$$\Delta J_{reflection\ loss} = \frac{q}{hc}\int_{\lambda_1}^{\lambda_2} \lambda \cdot R(\lambda)P(\lambda)d\lambda \tag{4.55}$$

where $R(\lambda)$ is the front reflection of the AR coating, and $P(\lambda)$ is the incoming power density from AM1.5 spectrum. The weighted average reflectance R_{ave} for the partial spectrum of interest is considered as a quality indicator for the AR coating design:

$$R_{ave} = \frac{\int_{\lambda_1}^{\lambda_2} \lambda R(\lambda)P(\lambda)d\lambda}{\int_{\lambda_1}^{\lambda_2} \lambda P(\lambda)d\lambda} \tag{4.56}$$

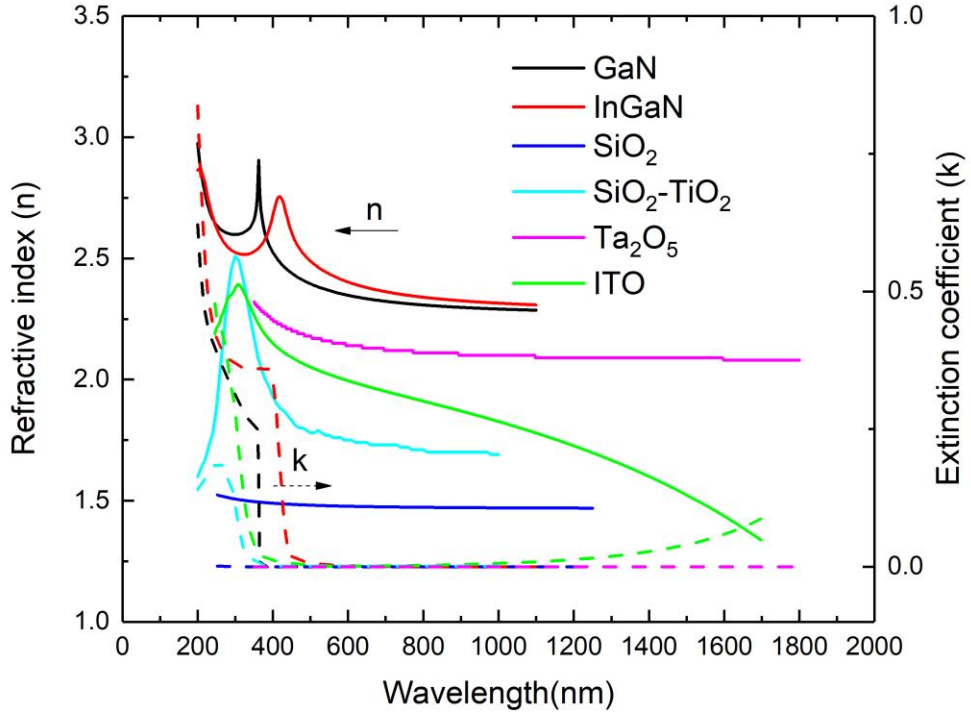

Figure 4.4 Optical constants of the materials used in the simulation. Solid lines represent the refractive index and the dash lines represent the extinction coefficient.

Figure 4.5 shows the front reflection calculated by TMM for different structures. The average front reflection, R_{ave}, for 300nm to 1200 nm spectrum for a bare GaN substrate is about ~16.7%, which could significantly reduce the short circuit current (Jsc) and degrades the performance of the device. Since less defective material should be grown first to minimize defect propagation, lower defects and higher conductivity n-type GaN serve as the substrate and base absorbers. This leads to p-GaN grown as the top emitter. p-GaN with more defects, which has low conductivity for lateral current transport to the contact fingers. In this regard, recently published research work shows ITO can serve as a better transparent

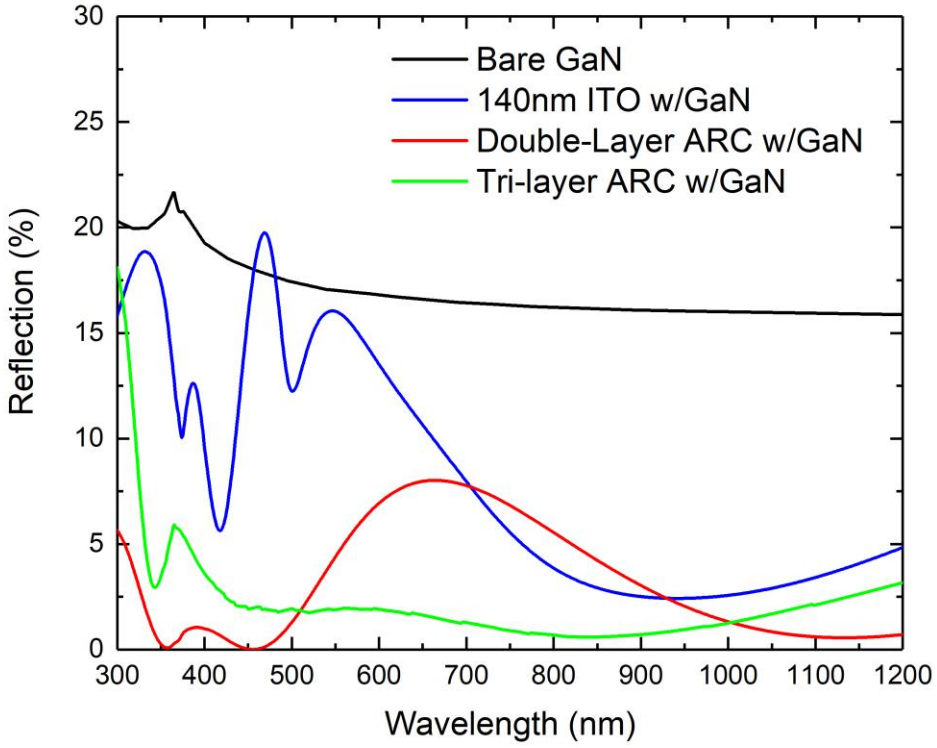

Figure 4.5 Comparison of the reflectance between a bare GaN substrate, 140nm ITO w/GaN, a double-layer ARC w/GaN and a tri-layer ARC w/GaN.

current spreading layer with lower lateral resistance[26], [29], [49]–[51]. More importantly, as shown in Figure 4.5, the refractive index of ITO is between GaN and the ambient air, making it a material candidate for nitride ARC design. With 140 nm ITO deposited on top of the device, the average reflection from 300 nm to 1200 nm reduces to ~7.8%. To further improve the performance of the ARC, a tri-layer ARC is adopted with 83 nm SiO_2, 50 nm SiO_2-TiO_2 and 56 nm Ta_2O_5. With the tri-layer ARC, the average reflection from 300 nm to 1200 nm was improved to 1.6%. So far, this work has shown ARC designs targeting a very wide solar spectrum from 300 nm to 1200 nm, which is applicable for multiple-

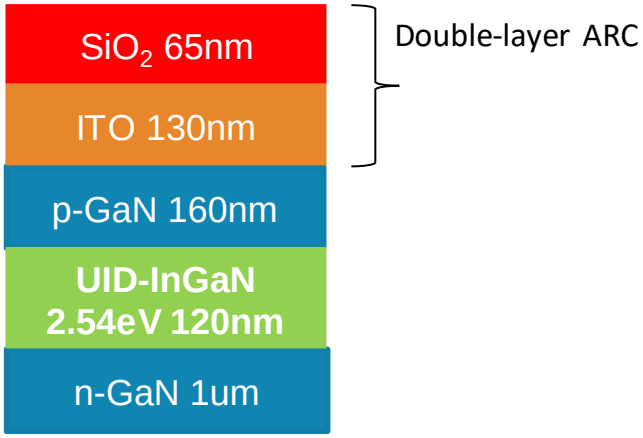

Figure 4.6 Schematic diagram of a 2.54 eV InGaN device with a double-layer ARC simulated at 500 C, 1 sun AM1.5. Thickness of the SiO_2 and the ITO has been optimized for the best solar response. The optimized thickness of SiO_2 and ITO is 65nm and 130nm, respectively.

junction solar cells and hybrid CST system. On the other hand, the wide bandgap 1J nitride cell fabricated to date demands an ARC tailored in a relatively short and narrow spectral range (300 nm to 500 nm). In that regard, a double-layer ARC is proposed for a lower cost and simpler design. This double-layer structure can leverage the ITO current spreading layer already deposited on the nitride cell in the existing technology. A double-layer ARC with 64 nm SiO_2 and 140 nm ITO is adopted with $\Delta J_{reflection\ loss}$ optimization. Compared with the tri-layer, average reflection from 300 nm to 1200 nm increases to ~3.85%. Although it is not as competitive as tri-layer within long-wavelength range (300 nm to 1200 nm), it provides a very low front reflection ~0.5% (compared with ~2.7% for tri-layer) in the very short wavelength range (300 nm to 500 nm) and makes it promising for wide bandgap nitride solar cell applications.

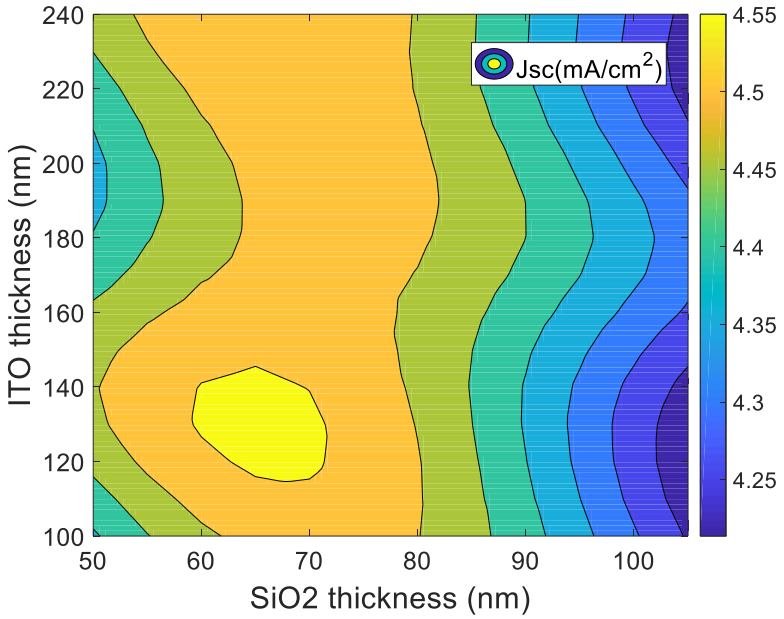

Figure 4.7 2D contour plot of the short-circuit current (Jsc) for the investigated devices as a function of ITO and SiO_2 thickness. The optimized thickness of the SiO_2 and ITO is 65nm and 130nm, respectively.

4.5 Validation from Silvaco Device Simulation in Batch Mode

In order to validate the in-house TMM solver, a 2.54 eV InGaN solar device with a double-layer ARC was simulated in Silvaco, Atlas in batch mode. As shown in Figure 16, it consists a 200-nm-thick, n-GaN bottom substrate layer, a 120-nm-thick, $10^{17}cm^{-3}$-n-doping UID-$In_xGa_{1-x}N$ base layer, and a 50-nm-thick, $10^{19}cm^{-3}$-doping p-GaN top layer. Thickness of SiO_2 and ITO have been varied for different devices. J_{sc} of the corresponding device has been optimized for the best ARC design. Since a good ARC design reflects less light at the front surface, it leads to more photons being absorbed and a higher photocurrent level. Figure 4.7 shows a 2D contour plot of the short-circuit current (Jsc) for the investigated devices as a function of ITO and SiO_2 thickness. Each ITO and SiO_2 thickness

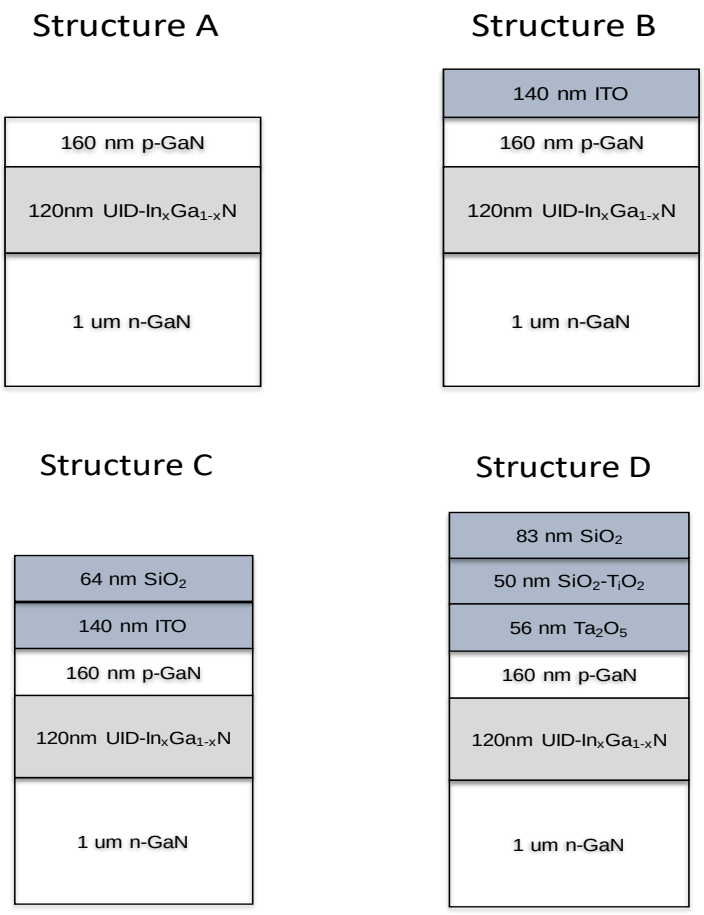

Figure 4.8 Schematic diagrams of a 2.54 eV standard InGaN solar device simulated for different ARC designs at 550 C, 1 sun. Structure A is the device without an AR-Coating. From Structure B to Structure C, one-layer ITO, double-layer and tri-layer ARC are added to the base device, separately for performance comparison.

(t_{SiO_2}, t_{ITO}) point in the 2D contour corresponds to a device numerically simulated in Silvaco Atlas. The optimized thickness of the SiO_2 and ITO was found to be 65nm and 130nm, respectively. This is consistent with the optimization results from in-house TMM solver which demonstrated that the optimized thicknesses of SiO_2 and ITO are 64 nm and 140 nm. Thus, this validation work demonstrates the in-house TMM solver is reliable for the ARC designs presented in this dissertation.

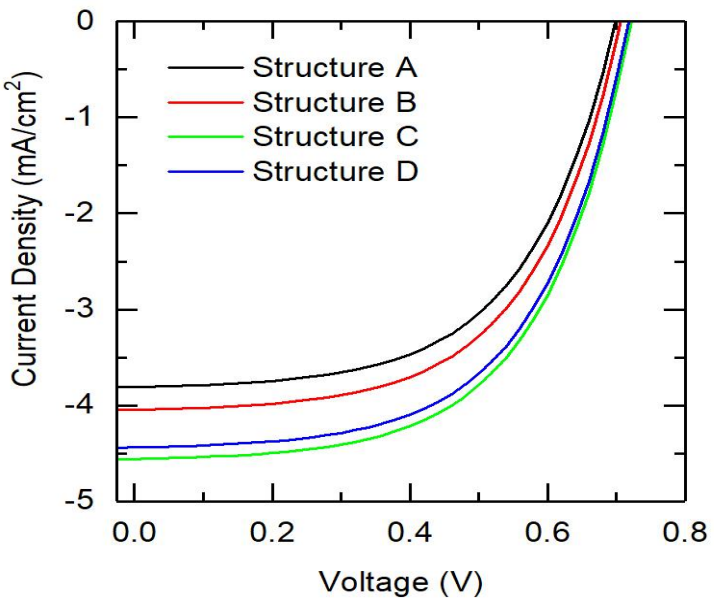

Figure 4.9 IV curves of InGaN devices with different ARCs simulated at 550 C, 1sun, as shown in Figure 4.8.

TABLE V
Summary of Jsc, Voc, FF and conversion efficiency simulation of a standard InGaN solar cell with different ARCs.

Structure	Jsc (mA/cm^2)	Voc (V)	FF	Efficiency (%)
A	3.80	0.698	0.510	1.52
B	4.04	0.706	0.574	1.64
C	4.56	0.721	0.579	1.90
D	4.44	0.717	0.577	1.83

4.6 Performance of the Proposed ARC Designs with PV Devices

In order to investigate the impact of the designed ARCs on the target InGaN solar cell, a 2.54 eV InGaN base device is numerically simulated with different ARCs via the transfer matrix method. As shown in Figure 4.8, Structure A is standard p-on-n

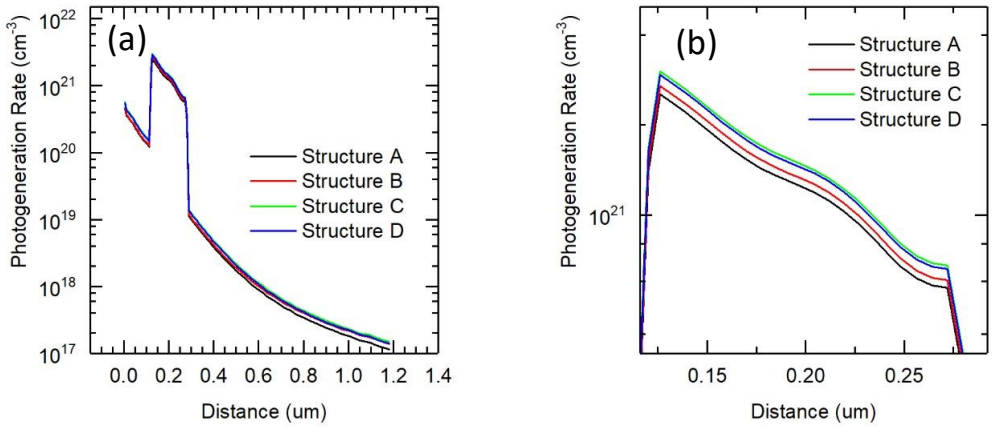

Figure 4.10 (a) Photo-generation rate as a function of device depth from the top p-GaN emitter to the bottom n-GaN substrate for devices from Structure A to Structure D. (b) A partially enlarged drawing of photo-generation rate in InGaN base absorber from (a).

InGaN/GaN solar cell with 2.54 eV base absorber. From Structure A to Structure B, a 140 nm ITO layer deposited on top of the device serves as both an ARC layer and a current spreading layer. Structure C represents a device coupled with the optimized double-layer ARC. For Structure D, an optimized tri-layer ARC is adopted and applicable for the hybrid CSP system due to its very low reflection over a wide spectrum range. Obviously, except for the difference of the ARC adopted for these four devices, the material properties of InGaN/GaN are identical. Thus, the IV response of the devices can be a measure of the optical performance for the designed ARC. Figure 4.9 shows the IV curves for the same device for four different ARCs. The corresponding solar cell characteristics such as Jsc, Voc, FF and efficiency are summarized in Table 5. Structure A shows the worst performance due to high front reflection loss. Structure C is found to be the champion device, since the double-layer ARC is optimized for a wavelength range from 300 nm to 500 nm. It corresponds to the bandgap 2.54 eV (488 nm) of the investigated device. From

Structure A to Structure C, Jsc increases from 3.80 mA/cm^2 to 4.56 mA/cm^2; V_{oc} also increases from 0.698 V to 0.721 V due to a larger light intensity; the FF increases from 0.51 to 0.574 together with V_{oc} improvement. It results in a increase of conversion efficiency from 1.52% to 1.9% at 550 C. Structure B shows that, with just one ITO layer, the efficiency could increase from 1.52% to 1.64%. From Structure C to Structure D, the efficiency just slightly decreases and makes it promising for a hybrid CSP converter since it targets for very wide range spectrum. Figure 20 shows the photo-generation rate as a function of device depth from top p-GaN emitter to bottom n-GaN substrate for devices from Structure A to Structure D. The optical intensity for a given depth x into the device is given by the following equation:

$$\mathrm{I(x)} = \mathrm{I}(0)e^{-\alpha x} \tag{4.57}$$

where $\mathrm{I}(0)$ is the incoming optical intensity at top surface of the device and α is the absorption coefficient for the corresponding material in the device. The absorption coefficient α generally is a function of the photon wavelength (or energy).

For a device exposed to the solar spectrum, the total optical generation rate can be described as follows:

$$G(x) = \sum \frac{\alpha_i}{E_i} \mathrm{I}(0)e^{-\alpha_i x} \tag{4.58}$$

where E_i is the photon energy in the spectrum, α_i is the corresponding absorption coefficient for the given photon energy. It explains the reason that the optical generation rate exponentially decays with device depth in both the GaN and InGaN layers. Since the bandgap of InGaN in this simulation is smaller than GaN's (3.42 eV), the photo-generation rate of the InGaN layer in the device is much larger than the top GaN layer, and contributes most of the photo-carriers generated from this solar cell as shown Figure 4.10(a). Figure

4.10(b) shows a partially enlarged drawing of the photo-generation rate in the InGaN base absorber from Figure 4.10(a). It is obvious that with an ARC, the photo-generation rate is improved in the InGaN base absorber. Then more photo generated electron-hole pairs are created, which results in a larger Jsc, Voc, FF and energy conversion efficiency from the base device (Structure A) to the champion device (Structure C).

4.7 Summary

In this chapter, the ARC design for an InGaN solar cell has been extensively studied via an in-house TMM solver and the commercial package Silvaco Atlas. First, the classical electromagnetic theory for optical wave propagation in the medium-stacked structure has been reviewed. The transfer matrix method for light traversing between multiple-layer materials has been introduced. It includes calculation of the optical reflection and transmission at interfaces of different mediums. The optical intensity and photo-generation rate can be calculated elegantly via elements of the transfer matrix method. Second, this work reports a double-layer ARC targeting at the spectrum from 300 nm to 500 nm and a tri-layer ARC targeting at spectrum from 300 nm to 1200 nm. The former double-layer ARC is applicable for a InGaN 1J wide bandgap cell with interest on performance of the PV cell itself. The latter triple-layer ARC demonstrates very low front reflection loss over a wider spectrum range, which make it promising for application for multiple-junction cell and hybrid CSP converters.

Thirdly, the optimization of a double-layer ARC from a in-house TMM solver has been validated in Silvaco Atlas. Around 500 devices are simulated in Atlas batch mode, which leads to the optimized of J_{sc} for 65 nm of SiO_2 and, 130 nm of ITO. It is very close to the results obtained by the in-house TMM solver in which reflection loss photo-current is to

be minimized. Finally, IV characteristics of 2.54 eV InGaN devices with different ARCs have been investigated with numerical simulation. Both devices with double-layer and tri-layer ARCs show better performance, especially in Jsc and the efficiency compared with the base device without the ARC, to reduce front reflection loss. Photogeneration profiles of the investigated structures have also been plotted and demonstrate that more light will be absorbed for structures with an ARC.

CHAPTER 5

MULTIPLE QUANTUM WELL EFFECTIVE MOBILITY MODEL

The carrier transport dynamics inside a quantum well structure is complicated. It involves thermal escape, tunneling and cascade transport effects. The models from Silvaco Atlas are inadequate to include all these effects. Self-consistent simulation would be time-consuming for large stacks and complicated structures, making it difficult for such simulation to provide quick feedback for the device design. The research group from the University of Tokyo proposed a simplified carrier transport model in MQW devices using effective drift mobility approximation [52]. They found that the carrier averaged drift velocity has linear dependence on the internal field regardless of the complicated carrier transport dynamic inside MQW. This behavior is similar to carriers in bulk materials, allowing us to approximate the MQW region as a quasi-bulk material with a specific effective drift mobility.

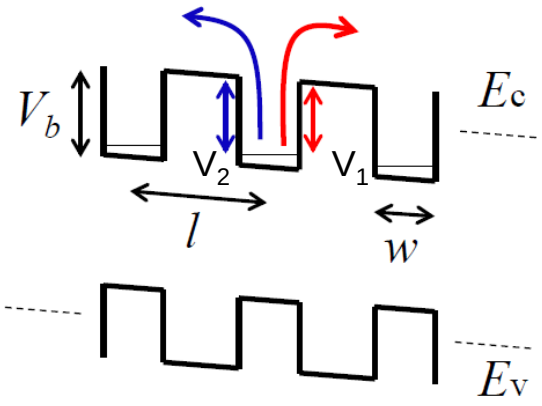

Figure 5.1 Electron transport in the MQW region: The blue curve corresponds to carrier escaping backward with barrier height V_2 and red curve corresponding to carriers escaping forward with barrier height V_1.

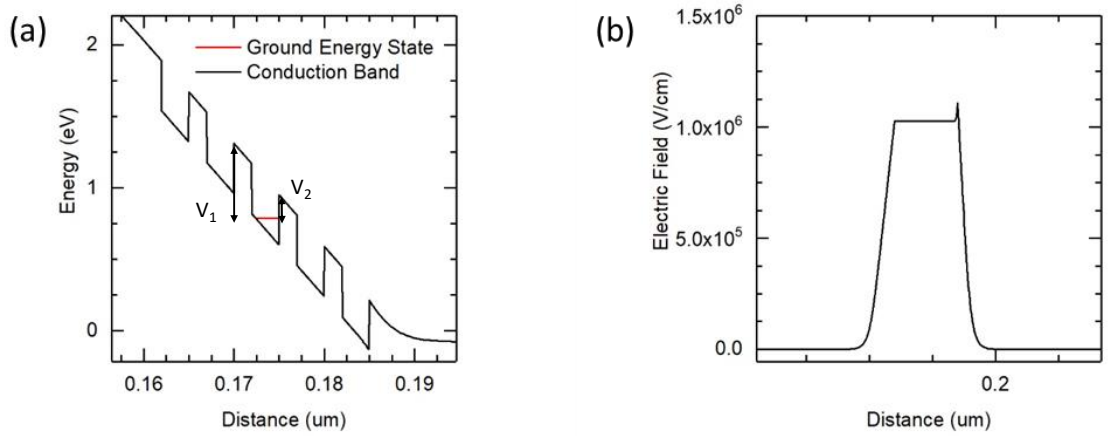

Figure 5.2 (a) Quantum confinement effects for electrons in the conduction band. V_1 and V_2 correspond to backward escape barrier and forward escape barrier, respectively. (b) Electric field along the device. The plateau part corresponds to the electric field E in MQW region. The simulation is at 300K. Polarization effects have not been included in above simulation.

Figure 5.1 shows the escape transport mechanism for carriers inside quantum well. The averaged drift velocity $\bar{v}$ can be expressed as below:

$$\bar{v} = l\left(\frac{1}{\tau_{esc,f}} - \frac{1}{\tau_{esc,b}}\right) \tag{5.1}$$

where l is the MQW period, $\tau_{esc,f}$ and $\tau_{esc,b}$ are the carrier escape time constants when moving forwards and backwards, respectively.

For thermal escape, the escape time constant τ_{esc} across a potential barrier of height V from the ground state is

$$\tau_{th} = \tau_{th0} e^{\frac{qV}{k_B T}} \tag{5.2}$$

where τ_{th0} is a factor related to the QW density of states[53].

Therefore, the averaged thermal escaping velocity is

$$\bar{v}_{th} = \frac{l}{\tau_{th0}}\left(e^{\frac{-qV_1}{k_B T}} - e^{\frac{-qV_2}{k_B T}}\right) \tag{5.3}$$

where V_1 and V_2 are the escape forward and backward barrier heights, respectively.

For tunnel escape, the escape time constant τ_{tun} calculated from the WKB approximation [54] is

$$\tau_{tun} = \tau_{tun0} e^{\frac{2}{\hbar}\int_0^b \sqrt{2m_b^* q(V-Ez)dz}} \tag{5.4}$$

where τ_{tun0} is the carrier oscillating time inside QW, m_b^* is the effective mass of the barrier material and *b* is the barrier thickness. Thus, the averaged velocity for the tunnel escape velocity is

$$\bar{v}_{tun} = \frac{l}{\tau_{tun0}} [e^{-\frac{2}{\hbar}\int_0^b \sqrt{2m_b^* q(V_1-Ez)dz}} - e^{-\frac{2}{\hbar}\int_0^b \sqrt{2m_b^* q(V_2+Ez)dz}}] \tag{5.5}$$

Finally, the total averaged velocity can be expressed as

$$\bar{v} = \bar{v}_{th} + \bar{v}_{tun} \tag{5.6}$$

The mobility can be derived from $\bar{v}$ as the function of the *E* field.

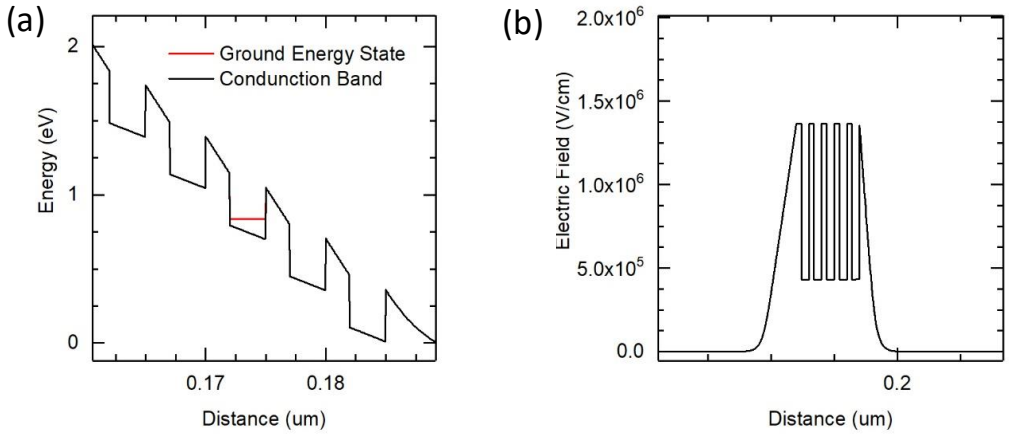

Figure 5.3 (a) InGaN MQW quantum confinement effect for electrons in conduction band (b) Electric field profile along MQW region with polarization effect.

A field dependent mobility model based on the Schrodinger-Poisson solver from Silvaco, Atlas is implemented for further quasi-bulk device simulation. The applied bias is varied

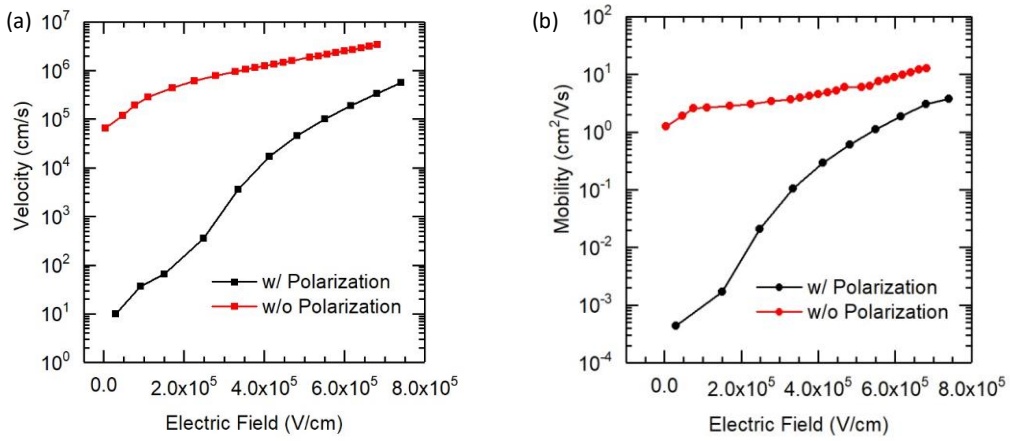

Figure 5.4 (a) Escaping velocity as a function of electric field for electrons with and without polarization effect. (b) From the derivative of (a), an electric field dependent mobility model for electrons is obtained with and without polarization effect.

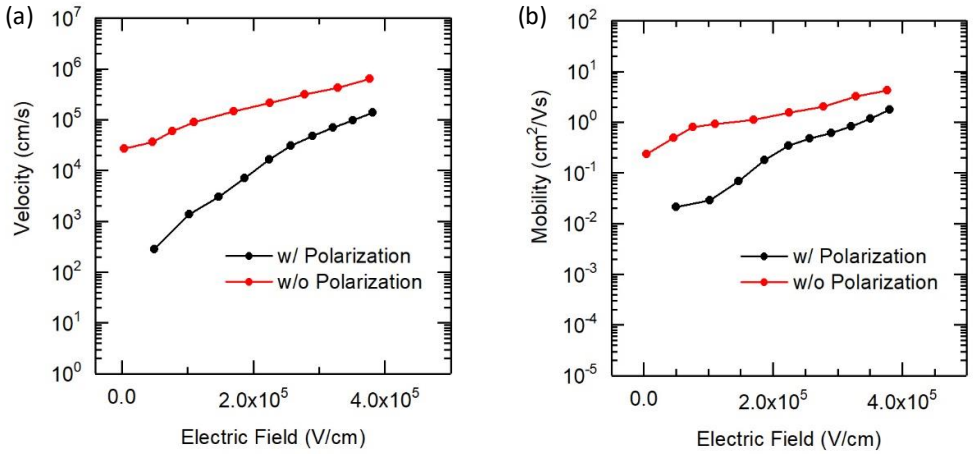

Figure 5.5 (a) Escape velocity as a function of electric field for holes with and without polarization effects. (b) From the derivative of (a), an electric field dependent mobility model for holes is obtained with and without polarization effects.

from 0 to V_{oc}, then electric field, ground state energy levels, and barrier height (V_1, V_2) can be extracted from device solution as shown in Figure 5.2. Substitute (V_1, V_2, E) into Equations 5.3, 5.5 and 5.6, to get escape velocity from QW as a function of E field can be calculated. Then the mobility as a function of E field can be obtained from the derivative

of the function $\bar{v}(E)$. The above model was originally designed for GaAs solar cell, thus polarization has not been included and it is not adequate for InGaN solar cell simulation.

In this work, we has upgraded this model for nitride solar cell simulation with polarization effects. A MQW structure with a 3nm GaN barrier and a 2nm InGaN well has been investigated for model development. As shown in Figure 5.3(a), the slope of he energy versus distance in the barriers is not the same as in the wells. This is because the polarization-induced electric field oppositely influences the field in barriers and wells as shown in Figure 5.3(b). The electric field, $E_{barrier}$, in the GaN barriers and, E_{well}, InGaN wells can be given by

$$\mathrm{E}_{barrier} = \mathrm{E} + \mathrm{E}_{Polar} \tag{5.7}$$

$$\mathrm{E}_{well} = \mathrm{E} - \mathrm{E}_{Polar} \tag{5.8}$$

where E_{Polar} is the polarization-induced electric field and E is the intrinsic electric field from built-in potential of the pin junction.

For the thermal escape velocity calculation, Equation 5.3 is still valid. However, for the tunneling escape velocity calculation, $\mathrm{E}_{barrier}$ should be used. The electron mobility as a function of E field is obtained from the derivative of the function $\bar{v}$ (E) in Figure 5.4. As shown in Figure 5.4(b), compared with bulk materials, the mobility for MQW without polarization effects is as low as ~1 cm^2/Vs at low field domain due to quantum confinement effects. With polarization effects, the magnitude at low field is further decreased to ~10^{-3} cm^2/Vs. The same technique is adopted for holes in valence band confinement effect. The Mobility model for holes is calculated as in Figure 5.5. In fact, bulk mobility electrons and holes are ~1000 cm^2/Vs and ~100 cm^2/Vs, respectively. The large degradation of the MQW effective mobility is originated from quantum confinement and polarization effect.

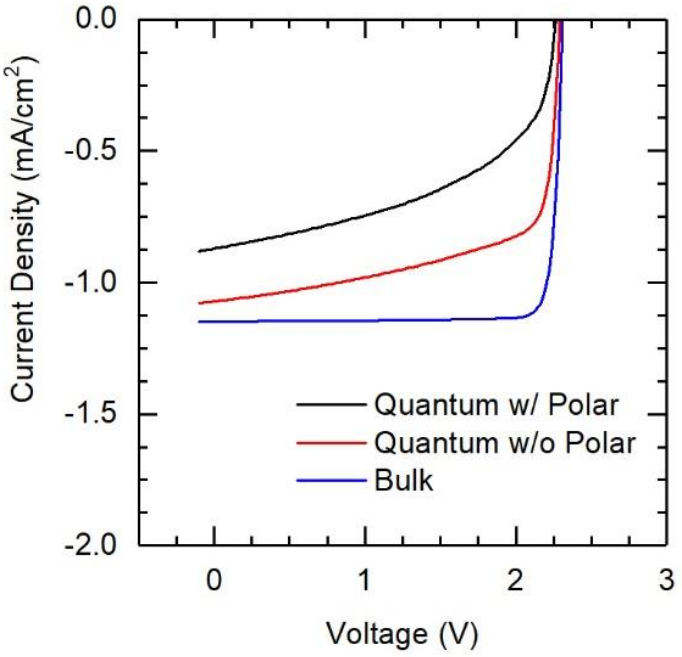

Figure 5.6 IV curves of the quasi-bulk simulation for MQW device with different mobility models: bulk, quantum confinement without polarization and quantum confinement with polarization. (300K, 1 sun)

Thus, the electric field dependent MQW effective mobility model are established and can be adopted for quasi-bulk device simulation.

With the established effective mobility model, one can start the IV simulations for InGaN/GaN MQW devices as shown in Figure 2.12. The 40-periods standard MQW device has been simulated in a quasi-bulk configuration with different mobility models. 40 periods

TABLE VI
Summary of Solar Characteristics with Different Mobility Models.

Mobility Models	Jsc (mA/cm^2)	Voc (V)	FF	Efficiency (%)
Bulk	1.15	2.31	0.89	2.3
Quantum w/o Polar	1.07	2.28	0.67	1.7
Quantum w/ Polar	0.87	2.26	0.50	1.0

of quantum wells were replaced with bulk InGaN material of the same thickness. Figure 5.6 shows the IV curves of the quasi-bulk simulation for MQW device with different mobility models: bulk, quantum confinement without polarization and quantum confinement with polarization. With all the parameters summarized in Table 6, it shows that due to quantum confinement effect, the efficiency decreases from 2.3% of bulk to 1.7% of quantum. Together with the polarization effects, efficiency finally degrades to 1.0%. In fact, J_{sc}, V_{oc}, and *FF* all degrade with quantum confinement and polarization. Among those factors, the *FF* degradation dominates the efficiency loss. This is because both quantum confinement and polarization effects suppress the photo-carrier collection and increases the series resistance of the device, thus resulting in a smaller FF.

CHAPTER 6

CONCLUSION AND FUTURE WORKS

In conclusion, this work has been performed to understand the behavior of InGaN photovoltaic devices at high temperatures via numerical simulation. With an effort to design high temperature InGaN concentrator solar cells, the electrical and optical performance were investigated based on modeling to assist the material growth and device process. A 1J solar cell, 2J tandem cell, multiple quantum well device, ARC design and an effective quantum mobility model have been studied in details in this dissertation.

First, 1J InGaN/GaN solar cells have been studied for polarization and band-offset effect. Band engineering techniques were used to suppress the potential barrier preventing carrier transport in the cell. Rather than a graded layer which is challenging to growth, a simple inter-layer with half indium mole fraction of the InGaN base was added at the hetero-interface. The layer can successfully relax the potential barrier in the conduction band (blocking electrons) and the valence band (blocking holes). Assisted by thermionic emission and tunneling effects at high temperatures, the band-engineered 1J GaN/InGaN cell overcomes the detrimental polarization effects. Furthermore, this work shows that the base doping and thickness should be optimized for best solar performance. High crystal quality (longer SRH lifetime) and concentration are required for V_{oc} recovery at high temperature, which leads to promising high efficiency solar performance. For a 100 ns SRH lifetime and 1000 suns (concentration), the efficiency has been improves from 8.8% (5ns, 1sun) to 19.6%. An alternative configuration for the 1J top cell is to leverage the MQW structure used in LED technology. Growing thick and high crystal quality InGaN absorber layers with a relatively high Indium composition is very difficult due to the large

lattice mismatch between InN and GaN. With MQW structures, the material quality of the InGaN absorber in each period can be improved. Fabricated InGaN MQW devices at ASU have demonstrated stability at high temperature and high concentration. Simulation shows good agreement with the measured data.

Secondly, a polarization engineering tunnel diode has been designed with decreased tunneling resistance. The tunneling current is improved by using a thin small bandgap InGaN layer sandwiched between heavily doped p an n GaN layers. A smaller bandgap of InGaN compared with GaN and band bending due to polarization effects at the hetero-interface decrease the tunneling distance and make tunneling more pronounced. With a low resistance tunneling junction and an optimized 1J cell, a tandem cell design was demonstrated. Current matching design methodology is shown for a monolithic MJ solar cell. Light trapping provides on its advantage for improving of both J_{sc} and V_{oc} with a thinner base InGaN absorber. Three pathways, such as a monolithic MJ device, a mechanical MJ device and a novel device design with tunnel junctions splitting a 1J cell into several similar bandgap sub-cells was proposed to achieve ~25% efficiency at 450 °C, 200 X suns.

Thirdly, optical management such as ARC design was studied in this work. A TMM solver has been adopted for reflection and transmission calculation in multiple-layer ARC designs. We propose a double-layer ARC targeting at the spectrum from 300 nm to 500 nm and a tri-layer ARC targeting for the spectrum from 300 nm to 1200 nm, separately. The former double-layer ARC is applicable for the InGaN 1J wide bandgap cell with interest on the performance of the PV cell itself. The latter triple-layer ARC demonstrates very low front

reflection loss in a wider spectrum range which make it promising for application on multiple-junction cell and hybrid CSP converters.

Finally, since multiple quantum well device simulation requires including complex physics models and is very time-consuming, an effective mobility model has been developed for InGaN solar devices that could be adopted for fast quasi-bulk device simulation.

For future work, since ideal Bragg-reflector is assumed for optical management in MJ solar cell configurations, there are research and development work to be done in that area. A practical Bragg-reflector should be well designed to the goal of reflecting the short wavelength spectrum back to the top and transmit the long wavelength spectrum into bottom. Moreover, with the developed effective mobility model for MQW solar cell devices, one can optimize the device based on device parameters such as its indium mole fraction, well/barrier thickness and quantum well quantity, etc.

REFERENCES

[1] International Energy Agency, *Solar Energy Perspectives*. OECD Publishing, 2011.

[2] H. M. Branz, W. Regan, K. J. Gerst, J. B. Borak, and E. a. Santori, "Hybrid solar converters for maximum exergy and inexpensive dispatchable electricity," *Energy Environ. Sci.*, vol. 8, no. 11, pp. 3083–3091, 2015.

[3] A. Luque and A. Martí, "Limiting efficiency of coupled thermal and photovoltaic converters," *Sol. Energy Mater. Sol. Cells*, vol. 58, no. 2, pp. 147–165, 1999.

[4] P. Herfurth *et al.*, "GaN-on-insulator technology for high-temperature electronics beyond 400 °C," *Semicond. Sci. Technol.*, vol. 28, p. 74026, 2013.

[5] L. Zhao, T. Detchprohm, and C. Wetzel, "High 400 °C operation temperature blue spectrum concentration solar junction in GaInN/GaN," *Appl. Phys. Lett.*, vol. 105, no. 24, p. 243903, Dec. 2014.

[6] J. J. Williams *et al.*, "Development of high-band gap high temperature III-Nitride Solar Cell for integration with concentrated solar power technology," in *2016 IEEE 43nd Photovoltaic Specialist Conference (PVSC)*, 2016, pp. 3–5.

[7] S. J. Pearton *et al.*, "GaN electronics for high power, high temperature applications," *Mater. Sci. Eng. B*, vol. 82, no. 1–3, pp. 227–231, 2001.

[8] C. a. M. Fabien and W. A. Doolittle, "Guidelines and limitations for the design of high-efficiency InGaN single-junction solar cells," *Sol. Energy Mater. Sol. Cells*, vol. 130, pp. 354–363, Nov. 2014.

[9] I. Vurgaftman, J. R. Meyer, and L. R. Ram-Mohan, "Band parameters for III-V compound semiconductors and their alloys," *J. Appl. Phys.*, vol. 89, no. 11 I, pp. 5815–5875, 2001.

[10] J. Wu *et al.*, "Temperature dependence of the fundamental band gap of InN," *J. Appl. Phys.*, vol. 94, no. 7, p. 4457, 2003.

[11] G. F. Brown, J. W. Ager, W. Walukiewicz, and J. Wu, "Finite element simulations of compositionally graded InGaN solar cells," *Sol. Energy Mater. Sol. Cells*, vol. 94, no. 3, pp. 478–483, Mar. 2010.

[12] T. T. Mnatsakanov, M. E. Levinshtein, L. I. Pomortseva, S. N. Yurkov, G. S. Simin, and M. A. Khan, "Carrier mobility model for GaN," *Solid. State. Electron.*, vol. 47, no. 1, pp. 111–115, 2003.

[13] D. M. Caughey and R. E. Thomas, "Carrier Mobilities in Silicon Empirically Related to Doping and Field," *Proc. IEEE*, vol. 55, no. 12, pp. 2192–2193, 1967.

[14] K. Kumakura, T. Makimoto, and N. Kobayashi, "Mg-acceptor activation mechanism and transport characteristics in p-type InGaN grown by metalorganic vapor phase epitaxy," *J. Appl. Phys.*, vol. 93, no. 6, p. 3370, 2003.

[15] O. Ambacher *et al.*, "Two-dimensional electron gases induced by spontaneous and piezoelectric polarization charges in N- and Ga-face AlGaN/GaN heterostructures," *J. Appl. Phys.*, vol. 85, no. 6, pp. 3222–3233, 1999.

[16] J. Y. Chang and Y. K. Kuo, "Simulation of N-face InGaN-based p-i-n solar cells," *J. Appl. Phys.*, vol. 112, no. 3, pp. 1–21, 2012.

[17] S. W. Zeng, B. P. Zhang, J. W. Sun, J. F. Cai, C. Chen, and J. Z. Yu, "Substantial photo-response of InGaN p–i–n homojunction solar cells," *Semicond. Sci. Technol.*, vol. 24, no. 5, p. 55009, 2009.

[18] C. Boney *et al.*, "Growth and characterization of InGaN for photovoltaic devices," *Phys. Status Solidi Curr. Top. Solid State Phys.*, vol. 8, no. 7–8, pp. 2460–2462, 2011.

[19] S. C. Jain, M. Willander, J. Narayan, and R. Van Overstraeten, "III–nitrides: Growth, characterization, and properties," *J. Appl. Phys.*, vol. 87, no. 3, pp. 965–1006, 2000.

[20] A. G. Bhuiyan, K. Sugita, K. Kasashima, A. Hashimoto, A. Yamamoto, and V. Y. Davydov, "Single-crystalline InN films with an absorption edge between 0.7 and 2 eV grown using different techniques and evidence of the actual band gap energy," *Appl. Phys. Lett.*, vol. 83, no. 23, pp. 4788–4790, 2003.

[21] J. Wu *et al.*, "Unusual properties of the fundamental band gap of InN," *Appl. Phys. Lett.*, vol. 80, no. 21, pp. 3967–3969, 2002.

[22] J. Wu, W. Walukiewicz, K. Yu, and J. A. Iii, "Indium nitride: A narrow gap semiconductor," *Info:*, pp. 1–8, 2002.

[23] Z. Q. Li, M. Lestradet, Y. G. Xiao, and S. Li, "Effects of polarization charge on the photovoltaic properties of InGaN solar cells," *Phys. Status Solidi*, vol. 208, no. 4, pp. 928–931, Apr. 2011.

[24] O. Jani, I. Ferguson, C. Honsberg, and S. Kurtz, "Design and characterization of GaN/InGaN solar cells," *Appl. Phys. Lett.*, vol. 91, no. 13, p. 132117, 2007.

[25] R. Dahal, J. Li, K. Aryal, J. Y. Lin, and H. X. Jiang, "InGaN/GaN multiple quantum well concentrator solar cells," *Appl. Phys. Lett.*, vol. 97, no. 7, p. 73115, 2010.

[26] B. W. Liou, "Design and fabrication of In x Ga 1 − x N / GaN solar cells with a multiple-quantum-well structure on SiCN / Si (111) substrates," *Thin Solid Films*, vol. 520, no. 3, pp. 1–7, 2011.

[27] D. Holec, P. M. F. J. Costa, M. J. Kappers, and C. J. Humphreys, “Critical thickness calculations for InGaN/GaN,” *J. Cryst. Growth*, vol. 303, no. 1 SPEC. ISS., pp. 314–317, 2007.

[28] G. B. Stringfellow, “Microstructures produced during the epitaxial growth of InGaN alloys,” *J. Cryst. Growth*, vol. 312, no. 6, pp. 735–749, 2010.

[29] K. Y. Lai, G. J. Lin, Y. L. Lai, Y. F. Chen, and J. H. He, “Effect of indium fluctuation on the photovoltaic characteristics of InGaN/GaN multiple quantum well solar cells,” *Appl. Phys. Lett.*, vol. 96, no. 8, pp. 2008–2011, 2010.

[30] P. Perlin *et al.*, “Towards the identification of the dominant donor in GaN,” *Phys. Rev. Lett.*, vol. 75, no. 2, pp. 296–299, 1995.

[31] S. Strite, “GaN, AlN, and InN: A review,” *J. Vac. Sci. Technol. B Microelectron. Nanom. Struct.*, vol. 10, no. 4, p. 1237, 1992.

[32] J.-Y. Chang, S.-H. Yen, Y.-A. Chang, and Y.-K. Kuo, “Simulation of High-Efficiency GaN/InGaN p-i-n Solar Cell With Suppressed Polarization and Barrier Effects,” *IEEE J. Quantum Electron.*, vol. 49, no. 1, pp. 17–23, Jan. 2013.

[33] A. G. Bhuiyan, K. Sugita, A. Hashimoto, and A. Yamamoto, “InGaN solar cells: Present state of the art and important challenges,” *IEEE J. Photovoltaics*, vol. 2, no. 3, pp. 276–293, 2012.

[34] Silvaco Inc, *Atlas User ’ s Manual*. 2016.

[35] D. L. Scharfetter and H. K. Gummel, “Large-Signal Analysis of a Silicon Read Diode Oscillator,” *IEEE Trans. Electron Devices*, vol. 16, no. 1, pp. 64–77, 1969.

[36] D. Vasileska, S. M. Goodnick, and G. Klimeck, *Computational Electronics: Semiclassical and Quantum Device Modeling and Simulation*. CRC Press, 2010.

[37] Y. C. Shen, G. O. Mueller, S. Watanabe, N. F. Gardner, a. Munkholm, and M. R. Krames, “Auger recombination in InGaN measured by photoluminescence,” *Appl. Phys. Lett.*, vol. 91, no. 14, p. 141101, 2007.

[38] M. Nawaz and A. Ahmad, “A TCAD-based modeling of GaN/InGaN/Si solar cells,” *Semicond. Sci. Technol.*, vol. 27, no. 3, p. 35019, Mar. 2012.

[39] W. Shockley and H. J. Queisser, “Detailed balance limit of efficiency of p-n junction solar cells,” *J. Appl. Phys.*, vol. 32, no. 3, pp. 510–519, 1961.

[40] P. Kozodoy *et al.*, “Heavy doping effects in Mg-doped GaN,” *J. Appl. Phys.*, vol. 87, no. 4, pp. 1832–1835, 2000.

[41] S. Krishnamoorthy, F. Akyol, P. S. Park, and S. Rajan, “Low resistance

GaN/InGaN/GaN tunnel junctions," *Appl. Phys. Lett.*, vol. 102, no. 11, p. 113503, 2013.

[42] S. Krishnamoorthy, P. S. Park, and S. Rajan, "Demonstration of forward inter-band tunneling in GaN by polarization engineering," *Appl. Phys. Lett.*, vol. 99, no. 23, p. 233504, 2011.

[43] J.-Y. Chang, S.-H. Yen, Y.-A. Chang, B.-T. Liou, and Y.-K. Kuo, "Numerical Investigation of High-Efficiency InGaN-Based Multijunction Solar Cell," *IEEE Trans. Electron Devices*, vol. 60, no. 12, pp. 4140–4145, Dec. 2013.

[44] E. Yablonovitch and G. D. Cody, "Intensity Enhancement in Textured Optical Sheets for Solar-Cells," *IEEE Trans. Electron Devices*, vol. 29, no. 2, pp. 300–305, 1982.

[45] X. M. Cai, S. W. Zeng, and B. P. Zhang, "Fabrication and characterization of InGaN p-i-n homojunction solar cell," *Appl. Phys. Lett.*, vol. 95, no. 17, pp. 1–4, 2009.

[46] L. J.-H. Lin and Y.-P. Chiou, "Optical design of GaN/In_xGa_1-xN/cSi tandem solar cells with triangular diffraction grating," *Opt. Express*, vol. 23, no. 11, p. A614, Jun. 2015.

[47] L. A. A. Pettersson, L. S. Roman, and O. Inganäs, "Modeling photocurrent action spectra of photovoltaic devices based on organic thin films," *J. Appl. Phys.*, vol. 86, no. 1, p. 487, 1999.

[48] S.-Y. Lien, D.-S. Wuu, W.-C. Yeh, and J.-C. Liu, "Tri-layer antireflection coatings (SiO2/SiO2–TiO2/TiO2) for silicon solar cells using a sol–gel technique," *Sol. Energy Mater. Sol. Cells*, vol. 90, no. 16, pp. 2710–2719, 2006.

[49] Y. J. Lee, M. H. Lee, C. M. Cheng, and C. H. Yang, "Enhanced conversion efficiency of InGaN multiple quantum well solar cells grown on a patterned sapphire substrate," *Appl. Phys. Lett.*, vol. 98, no. 26, pp. 2009–2012, 2011.

[50] C. L. Tsai, G. S. Liu, G. C. Fan, and Y. S. Lee, "Substrate-free large gap InGaN solar cells with bottom reflector," *Solid. State. Electron.*, vol. 54, no. 5, pp. 541–544, 2010.

[51] J. P. Shim, M. Choe, S. R. Jeon, D. Seo, T. Lee, and D. S. Lee, "InGaN-based p-i-n solar cells with graphene electrodes," *Appl. Phys. Express*, vol. 4, no. 5, pp. 4–7, 2011.

[52] K. Toprasertpong, T. Inoue, K. Watanabe, T. Kita, M. Sugiyama, and Y. Nakano, "Effective drift mobility approximation in multiple quantum-well solar cell," 2016, vol. 9743, p. 974315.

[53] H. Schneider and K. V. Klitzing, "Thermionic emission and Gaussian transport of

holes in a GaAs/AlxGa1-xAs multiple-quantum-well structure," *Phys. Rev. B*, vol. 38, no. 9, pp. 6160–6165, 1988.

[54] A. Larsson, P. A. Andrekson, S. T. Eng, and A. Yariv, "Tunable Superlattice pin Photodetectors: Characteristics, Theory, and Applications," *IEEE J. Quantum Electron.*, vol. 24, no. 5, pp. 787–801, 1988.